Anion Exchange Membranes Incorporating Multi N -Spirocyclic Quaternary Ammonium Cations via Ultraviolet-Initiated Polymerization for Zinc Slurry-Air Flow Batteries

Misgina Tilahun Tsehaye, Nak Heon Choi, Peter Fischer, Jens Tübke, Emilie Planes, Fannie Alloin, Cristina Iojoiu

Anion exchange membranes incorporating multi *N*-spirocyclic quaternary ammonium cations *via* UV-initiated polymerization for zinc slurry-air flow batteries

Misgina Tilahun Tsehaye[a], Nak Heon Choi[b,c], Peter Fischer[b], Jens Tübke[b,c], Emilie Planes[a], Fannie Alloin[a]*, Cristina Iojoiu[a]*

[a] Univ. Grenoble Alpes, Univ. Savoie Mont Blanc, CNRS, Grenoble INP, LEPMI, 38 000 Grenoble, France

[b]Applied Electrochemistry, Fraunhofer Institute for Chemical Technology ICT, Joseph-von-Fraunhofer, Straße 7, 76327 Pfinztal, Germany

[c]Institute for Mechanical Process Engineering and Mechanics, Karlsruhe Institute of Technology KIT, Straße am Forum 8, 76131 Karlsruhe, Germany

Corresponding authors*: Fannie.Alloin@lepmi.grenoble-inp.fr Cristina.iojoiu@lepmi.grenoble-inp.fr

Abstract:

Four anion exchange membranes (AEMs) incorporating multi *N*-spirocyclic quaternary ammoniums *via* ultraviolet (UV)-curing method were prepared and tested as separators in Zinc (Zn) slurry-air flow batteries (referred to here as ZSAFBs), an environmentally friendly, high specific energy and low cost energy storage device. The multi *N*-spirocyclic cations chain was grafted to PPO backbone *via* a hexyl spacer and its chain length, and thus membrane ion exchange capacity was tunned by varying the molar ratio between the hexyl diallyl ammonium grafted on PPO and the diallyl piperidinium monomer. This rationally designed 3D polymer results in a membrane with well-developed phase separation morphology, as confirmed by atomic force microscopy, with high hydroxide ion conductivity and low zincate ion diffusion coefficient i.e., PO-6CH_2-3x membrane exhibited 19 mS/cm and 2.3 x 10^{-12} m^2/s at 20 °C, respectively. The membranes exhibited great alkaline stability, with PPO-6CH_2-3x showing less than 8% drop in ionic conductivity after two weeks of accelerated degradation test (1 M KOH, 60 °C). The ZSAFB cell assembled with PPO-6CH_2-3x membrane exhibited an excellent maximum power density (153 mW/cm^2), surpassing those of reported values, making it a very promising membrane material for rechargeable ZSAFBs.

Keywords: Zinc slurry-air flow battery, Anion exchange membrane, *N*-spirocyclic quaternary ammonium, Poly(phenylene oxide), UV irradiation

Highlights:

- Crosslinked AEMs incorporating *N*-spirocyclic cation *via* UV-curing prepared.
- Zincate ion crossover and hydroxide ion conductivity measured.
- Well-connected hydrophilic domains observed by AFM.
- AEMs incorporating *N*-spirocyclic cation are first applied in Zn-air flow battery.
- The PPO-6CH$_2$-3x-based cell achieved an impressive power density of 153 mW/cm^2.

Graphical Abstract

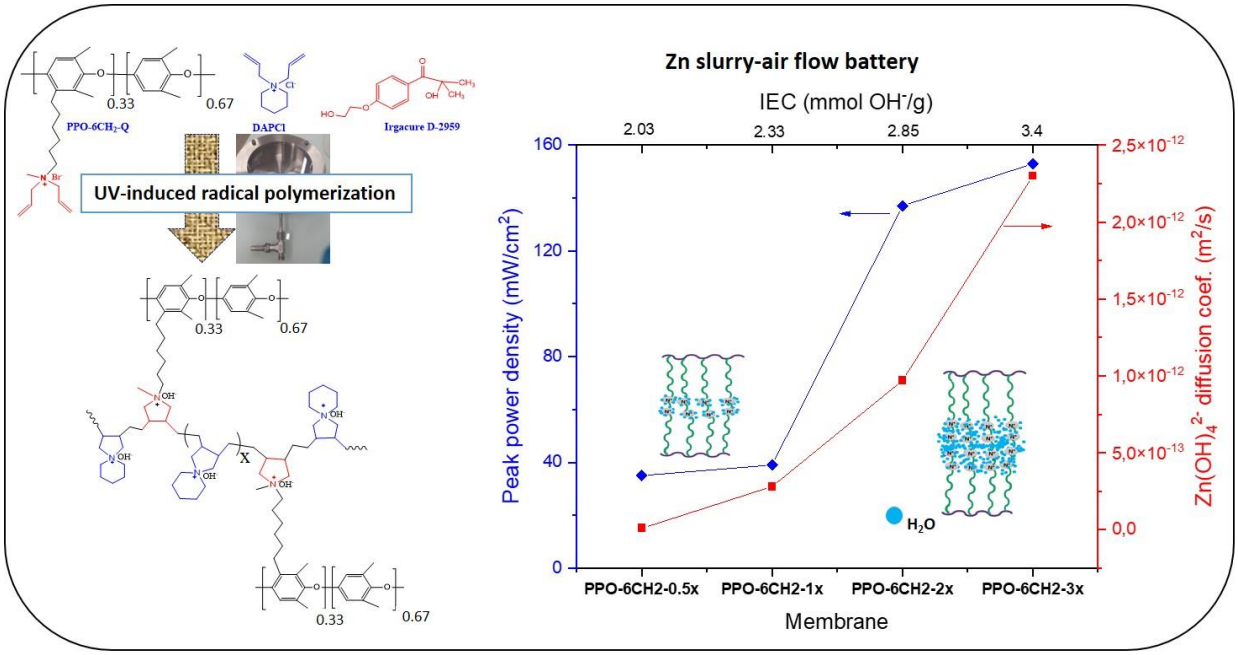

1. Introduction

Driven by the ever-growing greenhouse gas emissions, mainly CO_2, research directs to energy productions from 'greener' alternatives, such as wind and solar energy has recently received significant attention in the research community [1]. However, since they generate intermittent electrical power, there is a need for an energy storage device for optimal matching of energy demand and supply [2–5]. Currently, Li-ion [6] and Pb-acid [7,8] batteries are widely used energy storage systems; however, concerns over their safety and limited energy density require alternative energy storage devices [9–11].

Redox-flow batteries (RFBs) are promising alternatives because they decouple energy storage and power output to meet customer demand, have a long lifetime and can operate at ambient temperature and pressure

[12–15]. Among them is the Zinc (Zn) slurry-air RFB, a type of Zn-air battery which uses a suspension of Zn particles in aq. KOH electrolyte solution as the negative electrode and electrolyte. It is regarded as a potential energy storage technology due to its relatively high specific capacity, eco-friendliness, safety and inexpensive cost (wide abundance of Zn and O_2) [16,17]. In addition to the Zn slurry, the battery consists of a membrane and an air electrode.

The membrane in Zn slurry-air flow battery (ZSAFB) is used to conduct charge-carrying ions between the electrodes and avoid short circuit. The membrane should exhibit robust alkaline stability, high ionic (hydroxide, OH^-) conductivity and no or low zincate ($Zn(OH)_4^{2-}$) ion crossover to develop a long-term Zn slurry-air RFB. The utilization of porous membranes in Zn-air batteries [18] has been reported to result in in considerable $Zn(OH)_4^{2-}$ ion crossover [19], resulting in loss of capacity [20] and blockage of air electrode by the formed ZnO particles ($Zn(OH)_4^{2-} \rightarrow ZnO + H_2O + 2OH^-$). To reduce the $Zn(OH)_4^{2-}$ ion crossover, various porous membrane modification strategies, including ion-selective polymer coating [21–23] and nanoparticles filling [24] have been attempted. These, on the other hand, have been linked to a decrease in ionic conductivity.

Another possibility is to use anion exchange membranes (AEMs), which are regarded as promising candidates and are frequently proposed for use in Zn-air batteries [25,26]. An AEM containing a sulfonium cation was reported to show lower permeation of $Zn(OH)_4^{2-}$ ions than a Celgard® 5550 [27]. The Zn-air cell employing the prepared AEM showed six-fold higher discharge capacity than that of the polypropylene-based cell. Moreover, AEMs based on Poly(2,6-dimethyl-1,4-phenylene oxide) (PPO) and three different amines were fabricated and employed in primary Zn-air batteries [28]. Among them, the PPO-trimethylamine membrane had a $Zn(OH)_4^{2-}$ ion crossover of only 1.9×10^{-14} m^2/s, which was considered to be related to the membrane's proper ionic channels. Additionally, commercial AEMs, Tokuyama A201 [29,30] and Fumatech FAA-3 [31,32] have been tested in different Zn-air cells. However, despite the intriguing potential of AEMs for these batteries, it is still a relatively unexplored topic [18,19]. The correlation between AEM characteristics and Zn-air battery performance, in particular, has not been thoroughly investigated.

One of the biggest challenges for using AEMs in electrochemical applications, such as alkaline batteries, is alkaline stability[33–35]. Chemical instability of the fixed functional groups, polymer backbone and/or spacer can all cause chemical degradation of such ionomers. Cationic degradation, in particular, is regarded to be the primary reason why most present-day polymer-based AEMs rapidly degrade in alkaline conditions above 80 °C. Linear polyaromatic AEMs incorporating piperidinium and 6- azonia-spiro[5.5]undecane (ASU), an alkaline stable *N*-spirocyclic quaternary ammonium (QA) [36], cations *via* superacid-mediated polycondensation have been reported by Jannasch's research group [37,38]. The poly(terphenyl dimethyl-

piperidinium)-based AEMs showed no sign of degradation in 2 M NaOH at 60 °C for two weeks [37]. Moreover, Strasser *et al.* [39] prepared a multiblock AEM copolymers containing poly(diallylpiperidinum hydroxide) cation, which lost only 8% of its ionic conductivity after storage under harsh alkaline condition (1 M KOH, 80 °C) for 120 h. Recently, PPOs with 3,6-diazaspiro[5.5]undecane were prepared following two steps of quaternization method [40]. However, compared to ASU, the cation was reported to have inferior alkaline stability because of the cation's tertiary N atom which resulted in both Hofmann elimination and SN_2 substitution.

Another issue associated with alkaline stability of AEM is that AEMs quaternized in their benzylic positions (close to the polymer backbone) are sensitive towards chemical degradation, thus unstable especially in highly alkaline medium at high temperature [41]. Membranes with tethered benzyltrimethyl ammonium cations were reported to break into small pieces after 3 days, whereas comb-shaped AEMs retained their mechanical strengths in 1 M NaOH at 80 °C for 83 days [42]. Moreover, cations placed directly on the benzylic positions limit the ionic functions mobility and prevent phase separation, a prerequisite for highly conductive AEMs [43].

In this study, methyldiallylammonium groups were attached to a PPO *via* a 6-C long spacer (PPO-6CH_2-Q) to prevent benzylic position instability and facilitate phase separation. PPO was chosen for its high glass transition temperature, mechanical strength, chemical stability and low cost [44,45]. Furthermore, to overcome the difficulty of grafting *N*-spirocyclic quaternary ammonium cationic groups onto polymer backbone structures [39,46], ultraviolet (UV)-curing method is used to graft the *N*, *N*-diallylpiperidinium chloride (DAPCl) monomer onto the modified PPO polymer backbone. Multi-cation side chains have been reported to enhance the chemical stability and OH^- conductivity of ion exchange membranes [47]. In order to investigate the impact of ion exchange capacity (IEC) on water state, ionic conductivity, zincate ion crossover and battery performance, the monomer to PPO-6CH_2-Q polymer ratio was varied from 0.5 to 3. The prepared AEMs were tested for alkaline and thermal stabilities and characterized using atomic force microscopy and differential scanning calorimetry, which were used to investigate phase separation and water state in the membranes, respectively. Finally, the performance of the AEMs in ZSAFBs was studied by recording and comparing their polarization curves.

2. Experimental

2.1. Materials

Poly(2,6-dimethyl-1,4-phenylene oxide) (PPO, Polysciences Inc, Mn = 20,000 g/mol), chlorobenzene (Alfa Aesar, ACS reagent, ≥99.5%), 1,2-dichloroethane (Alfa Aesar, 99.8%), N-methyl-2-pyrrolidone (NMP, Alfa Aesar, reagent grade), allyl bromide (Alfa Aesar, 98%), allyl chloride (Alfa Aesar, 98%), chloroform (Alfa Aesar, 99.8%), Irgacure D-2959 (Ciba Specialty Chemicals Inc), methanol (Fisher Scientific, 99.9%), diallymethylamine (ABCR GmbH, 97%), chloroform (Fisher Scientific, 99.8%), piperidine (ABCR GmbH, ≥99%), 6-bromohexanoyl chloride (6-BHC, Sigma-Aldrich, 97%), diethyl ether (Sigma-Aldrich, 99+%), chloroform-d ($CDCl_3$-d, Sigma-Aldrich, 99.9% D), dimethyl sulfoxide-d_6 (DMSO-d_6, Acros Organics, 99.9%), aluminum chloride ($AlCl_3$, Acros Organics, 98.5%, anhydrous) and chlorobenzene (ABCR GmbH, ACS reagent, ≥ 99.5%) were used as supplied without any further purification.

2.2. Polymer synthesis

PPO-CO-Br: PPO with 6-C pendant chain (PPO-6CO-Br) was synthesized by slightly altering the method discussed elsewhere [48,49]. In a round bottom reaction flask, PPO (5 g) was dissolved in chlorobenzene (200 mL) and flushed with Ar. The reaction flask was kept at 0 °C for 30 mins before adding 6-BHC (9.6 mL) and $AlCl_3$ (2.5 g). Finally, the temperature was increased to room temperature (RT) for 24 h. The alkyl brominated PPO mixture was precipitated by using methanol, filtered and dried at 60 °C to obtain a white solid product (7.1 g). The degree of bromination/functionalization (around 33%) was evaluated using the ^{1}H NMR spectroscopy.

PPO-6CH$_2$-Br: The ketone groups in the PPO-6CO-Br polymer were reduced as follows. In a 350 mL heavy wall pressure vessel (pressure reactor purchased from chemglass), PPO-6CO-Br (1 g, 6.85 mmol ketone groups) was dissolved in 1,2-dichloroethane (40 mL), and then trifluoroacetic acid (40 mL**,** 685 mmol) and triethylsilane (4 mL, 68.5 mmol) were added. The reaction was performed, at 100 °C for 24 h, under pressure to prevent the solvent from evaporation and to raise the reaction temperature beyond the solvent-reactive mixture boiling point. The reaction mixture was neutralized with aq. KOH solution (30 wt. %, 100 mL) until the pH becomes neutral. The organic phase was then separated and precipitated using methanol. Subsequent dissolving in chloroform and re-precipitating in methanol were performed to remove the remaining triethylsilane and purify the obtained product. The collected polymer product (PPO-6CH$_2$-Br) was dried at 60 °C and its degree of ketone reduction was calculated using the ^{1}H NMR peak areas.

PPO-6CH$_2$-Q: The PPO-6CH$_2$-Br polymer was first dissolved in 5 wt. % NMP at 40 ^{o}C. To completely replace the bromine groups, methydiallylamine was added in excess (2.5 molar) and the reaction was allowed to run for 72 h. The quaternized polymer (PPO-6CH$_2$-Q) was collected by precipitation with diethyl ether and dried under vacuum (35 ^{o}C). The complete replacement of bromine atoms with the amine was confirmed using ^{1}H NMR. The protocol followed to prepare PPO-6CO-Br, PPO-6CH$_2$-Br and PPO-6CH$_2$-Q is shown in scheme I.

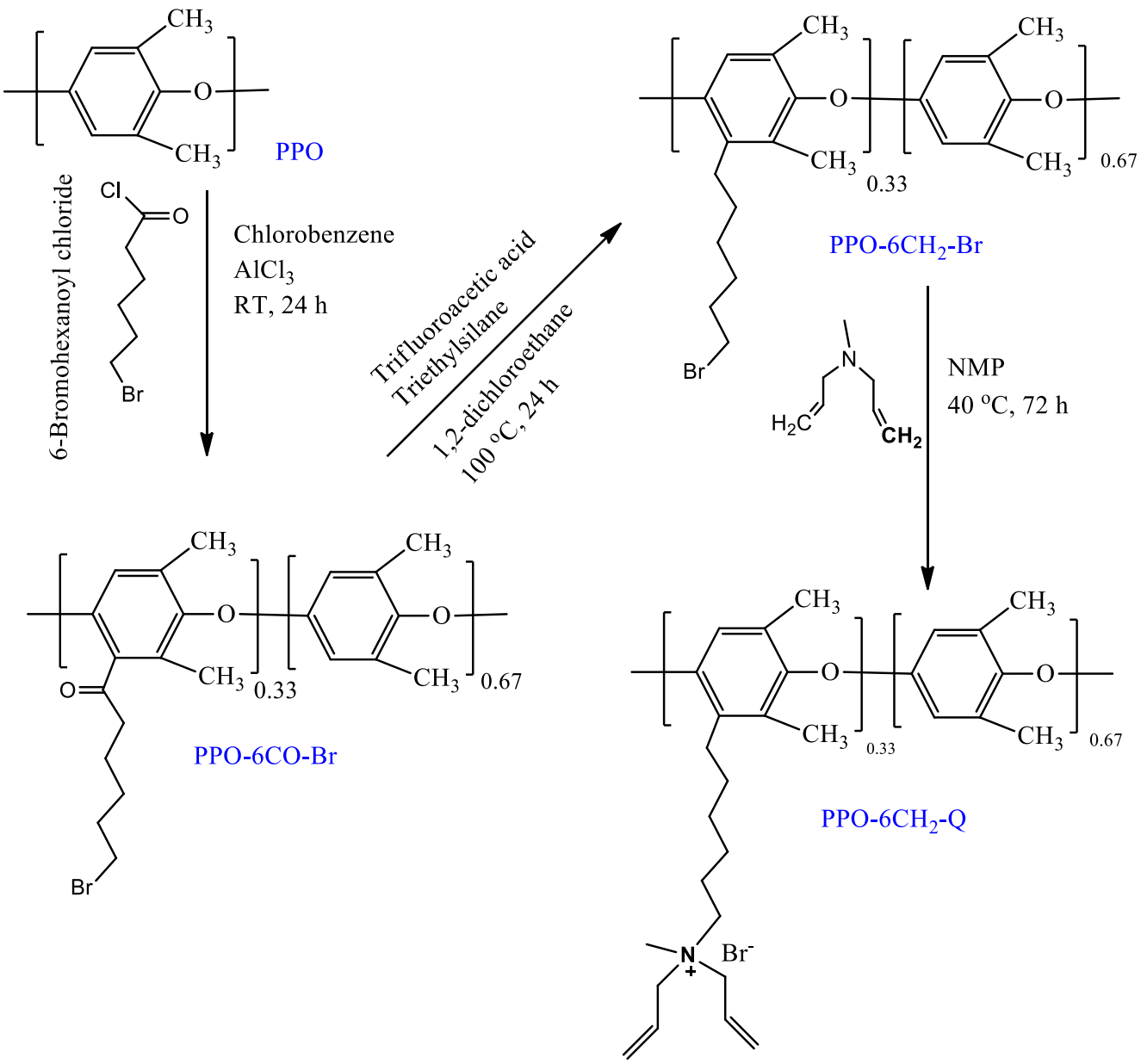

Scheme I: Schematic representation of PPO-6CO-Br, PPO-6CH_2-Br and PPO-6CH_2-Q polymers preparation.

2.3. *N*, *N*-Diallylpiperidinum chloride

DAPCl was prepared following a procedure previously published with slight modifications (Scheme II) [39,50]. First, 20 mL deionized (DI) water was added to a 250 mL reaction flask, followed by NaOH (12 g) at 0 °C. Once the mixture was completely dissolved, 25.54 g piperidine was added. Next, 26.3 mL allyl bromide was added dropwise, after which it was reacted at RT for 6 h. Separatory funnel was used to collect the oil

layer and chloroform was added to the aqueous layer remaining for one-time extraction. The chloroform was then removed by rotary vacuum evaporator. The product was neutralized by washing it with DI water, then drying it over Na_2SO_4 and filtering it with filter paper, with the remaining liquid product (*N*-allylpiperidine, 32.7 g) was collected for the following step. The yield was calculated to be 86%.

In the second step, the prepared *N*-allylpiperidine, allyl chloride (25.1 g) and DI water (60 mL) were added into a reaction flask. The reaction, protected with copper filament, was heated at 65 °C for two days. The oil part was then separated and poured into excess acetone, which was thoroughly stirred. Following a 48 h of drying at 40 ˚C, the solid DAPCl (32.8 g, 62% yield) was obtained.

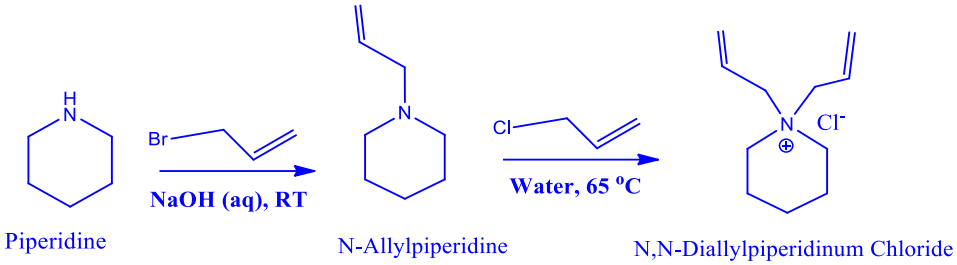

Scheme II. Schematic representation of DAPCl synthesis.

2.4. Membrane preparation

Four AEMs with different IECs were prepared using UV-initiated polymerization in a similar way to our previous study [51]. The membrane preparation was performed as follows. The appropriate amounts of each species (polymer, DAPCl monomer and initiator) were solubilized in a mixture of 1, 2-dichloroethane and NMP and the solutions are cast on a petri dish. The mixture solution was covered with aluminum foil with small holes to keep it out of the light and permit the 1,2-dichloroethane evaporation at RT. The film-containing petri dish was degassed to remove O_2. The viscous homogenous solution was cross-linked via UV-irradiation for 3 min under Ar. The membrane-containing petri dish was put in a 60 ˚C oven overnight. Following NMP evaporation, the AEM was collected and immersed in DI water to wash out any remaining solvents, monomers and non-grafted Poly(DAPCl). As shown in the Figure 1, the AEMs consists of pyrrolidinium and poly(5-azoniaspiro[4.5]decane) cations.

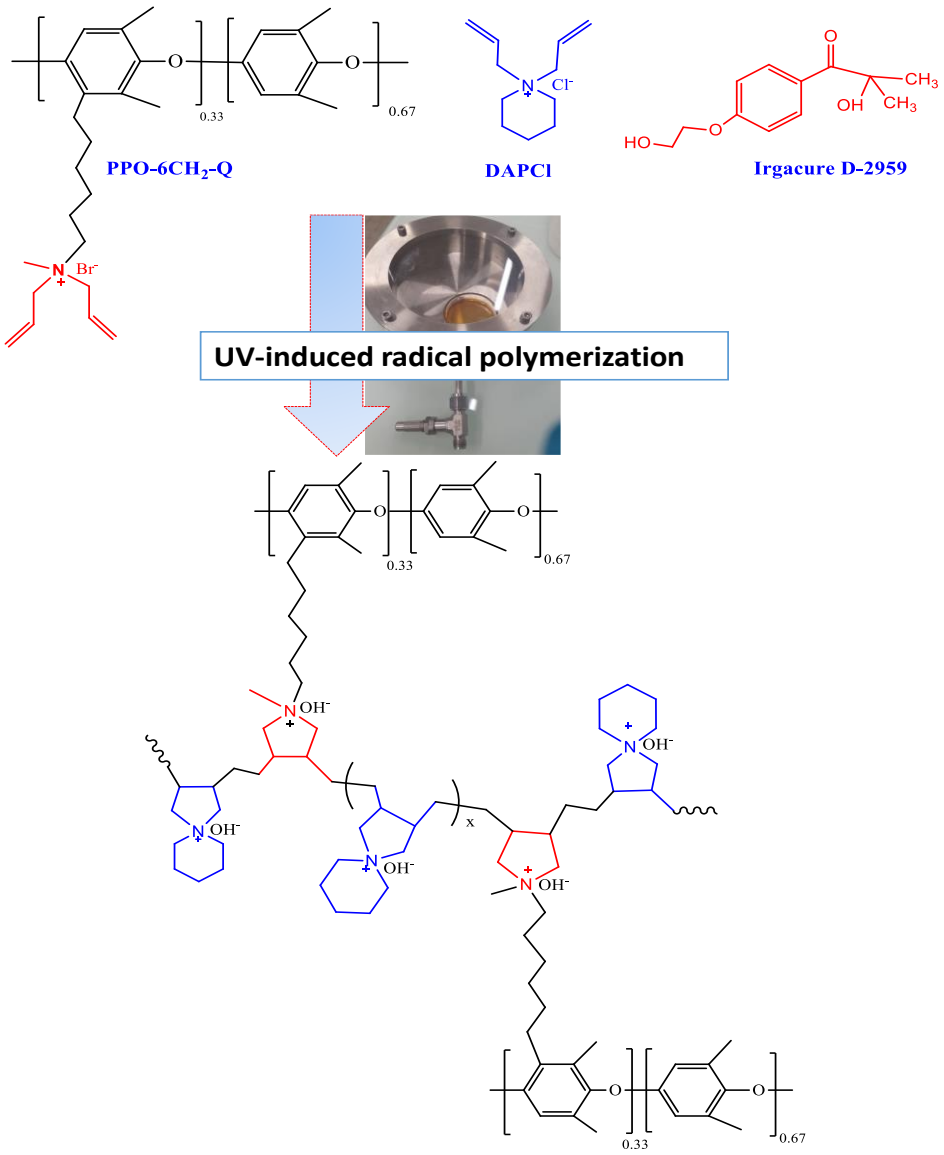

Figure 1: Schematic diagram of the AEM fabrication protocol.

2.5. Characterizations

2.5.1 Nuclear magnetic resonance (NMR)

^{1}H NMR spectra was recorded using a Bruker AV 400 NMR spectrometer using chloroform-*d* (δ ^{1}H = 7.26 ppm) or DMSO-d_6 (δ ^{1}H = 2.50 ppm) or D_2O (δ ^{1}H = 4.79 ppm).

2.5.2 Atomic force microscopy (AFM)

The surface morphology of the AEMs (OH^- form) was studied by tapping mode AFM analysis using Si probes (with a spring constant 5 N/m) and resonance frequency 60–80 kHz. The surface of the membranes was imaged immediately after adding a drop of DI water at RT and 40–60% relative humidity using Nanowizard (JPK) of CIME Nanotech platform (Grenoble, France). The height and phase images were taken at the same time in a hard tapping conditions, with a 0.7-0.8 ratio of A_{sp} to A_0 controlling the tip's interaction with the specimen. In these operating settings, phase images are recognized to contribute the most to morphology in these types of samples. The image processing was done with "Gwyddion" and the image analysis was done with "ImageJ" open-source software. Previously reported procedure [52] was used to identify the ionic and hydrophobic domains. Five images of PPO-6CH_2-3x membrane were evaluated.

2.5.3 Ion exchange capacity (IEC) and water uptake (WU)

The IECs of the AEMs were determined through Mohr titration method. The prepared AEMs were first converted to Br^- form by immersing in 1 M NaBr at 50 ^{o}C for two days. The membrane samples were then rinsed several times with DI water and dried at 50 °C overnight. The AEMs were weighed and transferred to $NaNO_3$ solution (0.2 M, 25 mL) for two days at RT. Three samples of the resultant solution were titrated with 0.01 M aq. $AgNO_3$, with K_2CrO_4 indicator. Finally, the IECs were calculated using equations (1 &2):

$$IEC_{Br-} = \frac{Volume \times Concentration\ of\ AgNO_3}{g\ dry\ membrane} = \frac{0.01 \times Volume\ \ AgNO_3}{g\ dry\ membrane} \quad (1)$$

$$IEC_{OH-} = \frac{IEC_{Br-}}{1-\frac{IEC_{Br-}(M_{Br-}-M_{OH-})}{1000}} = \frac{IEC_{Br-}}{1-0.0629 \times IEC_{Br-}} \quad (2)$$

The water uptake (WU) capacity of the membranes was determined gravimetrically from their wet and dry weights, as shown in equation (3):

$$WU(\%) = \frac{(Wet\ membrane\ weight - dry\ membrane\ weight)}{dry\ membrane\ weight} \times 100 \quad (3)$$

The reported IEC titration and WU of the AEMs are an average of at least three measurements.

The hydration number (λ) was estimated as follows equation (4):

$$\lambda = \left(\frac{W_{wet} - W_{dry}}{18.01}\right)\left(\frac{1000}{IEC \times W_{dry}}\right) = \frac{WU\ (\%) \times 10}{IEC \times 18.01} \quad (4)$$

2.5.4 Hydroxide and chloride ions conductivities

The Cl^- and OH^- ions conductivities (σ) of the membranes were determined by exchanging the resulting membranes in a saturated NaCl (1 M) and KOH (1 M), respectively, at RT for 24 h. The membranes were then washed with DI water. The ionic conductivities were determined (at RT*)* via a through-plane electrochemical impedance spectroscopy (EIS) in the frequency range 13 MHz – 5 Hz (equation 5). To avoid carbonation process, the AEM (OH^- form) resistance measurement was performed in a home-made glove-box under continuous Ar flow.

$$\sigma\ \left(\frac{S}{cm}\right) = \frac{\text{hydrated membrane thickness (cm)}}{\text{Membrane active area } (cm^2) \times Membrane\ resistance\ (\Omega)} \quad (5)$$

2.5.5 Differential scanning calorimetry (DSC)

The number (N) of bound or non-freezable water and bulky or freezable water in the AEMs were determined by DSC (Mettler-Toledo DSC1 instrument). AEM samples were immersed in water for a week. Wet membrane samples (approximately 10 mg), weighed after mopping their surface with tissue paper, were sealed in Al sample container. The thermal cycle was programmed to lower from RT to – 50 °C. It was followed by heating up to 25 °C at 5 K/min scan rate under N_2 (50 mL/min). The $N_{non\text{-}freezable}$ and $N_{freezable}$ were determined using equations 6 and 7:

$$N_{freezable} = \frac{M_{free}}{M_{tot}} \times \lambda = \frac{\Delta H_{free}/\Delta H_{ice}}{M_{tot}} \times \lambda \quad (6)$$

Where M_{tot} and M_{free} are the masses of the total and freezable water molecules, respectively. ΔH_{free} enthalpy is determined by integrating the area under the DSC peak. ΔH_{ice} is taken to be 334 J/g.

$$N_{non-freezable} = \lambda - N_{freezable} \quad (7)$$

2.5.6 Alkaline stability

The chemical degradation of the samples was determined by monitoring the changes in Cl^- ion conductivity after immersion in different alkaline solutions (6 M KOH at RT and 1 M KOH at 60 °C) during two weeks. Moreover, to simulate the practical ZSAFB application, the stability of the membranes in alkaline Zn slurry electrolyte at RT was studied.

2.5.7 Thermogravimetric analysis

Thermal properties of the membranes were determined by thermogravimetric analysis under N_2. Dry membrane samples were heated from RT to 800 °C with 10 °C/min heating rate.

2.5.8 Zincate ions crossover

A home-made diffusion cell was employed to quantitatively determine the zincate ion crossing through the prepared AEMs [20,21,28,53]. In this diffusion cell design, the enriched chamber contained 6 M KOH and $Zn(OH)_2$ (0.3 M, solubility limit at RT) and the depleted chamber contained only 6 M aq. KOH. The 0.5 cm^2 membrane was put between the chambers and atomic absorption spectroscopy (AAS) was used to quantify the amount of zincate ion on the depleted side. The diffusion coefficient (D) of zincate ion of each membrane was determined from the slope of time *vs* $ln(\frac{C_A}{C_A - C_B})$ plot. The zincate ion concentrations in the depleted and enriched sides are C_B (mol/L) and C_A (mol/L), respectively. Additionally, the ratio of ionic conductivity to zincate ion diffusion coefficient is used to estimate the membranes' permselectivity as follows (equation 8):

$$\text{Permselectivity} = \frac{\sigma_{OH-}}{D_{Zn(OH)_4 2-}} \quad (8)$$

2.5.9 Single Zn slurry-air cell assembly and electrochemical performance

A single Zn slurry-air cell containing air cathode, membrane and Zn slurry with a CuNi plate was used. The catalyst ink consists of Pt/C catalyst, FAA-3 ionomer (23 wt. %. of the catalyst layer, Fumatech), DI water and isopropanol. The Pt loading was 1 mg/cm^2. After 15 min of sonication in an ultrasonic water bath, the prepared suspension was sprayed over a gas diffusion layer (5 cm^2) (SGL Carbon, 29BC, Germany). The Zn slurry was prepared in the same manner as described in our previous study [54], and the battery electrochemical performance was tested as stated in that study.

The ZSAFB (Figure 2), employing the four prepared AEMs, performance was studied by current-voltage characteristic curves. EIS measurements were performed to determine the ohmic resistance of the battery with the various AEMs. The flow rates of the Zn slurry in the negative electrode and synthetic air in the air cathode were 160 and 100 mL/min, respectively.

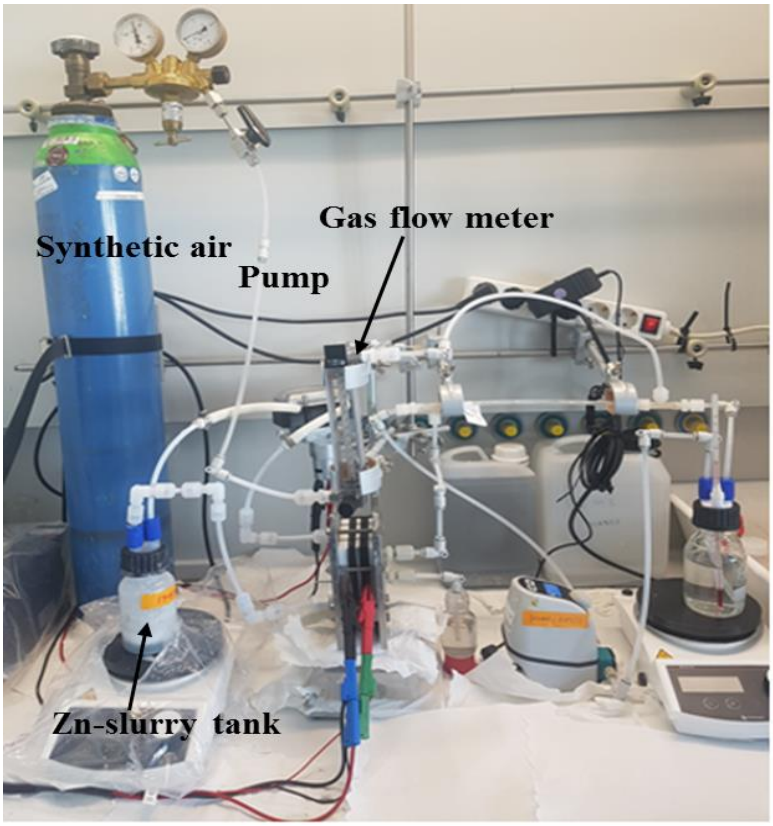

Figure 2: Image of the ZSAFB.

3. Results and discussion

3.1 Polymers and monomer preparation

The reaction protocol followed to prepare the polymer is summarized in scheme I. The bromination, ketone reduction and quaternization reaction products involved during the preparation of PPO-6CH_2-Q were confirmed using ^{1}H NMR. The bromination of PPO polymer with a 6-C spacer containing a ketone group in the benzylic position using 6-bromohexanoyl chloride in a Friedel–Crafts acylation was performed based on slight modification of the method discussed in the literature [48,49]. The peak at around 3.0 ppm (denoted as peak i) represents to the protons bonded to the carbon next to the ketone group. The bromination degree was determined from the proportion of the ^{1}H NMR integrals of protons in –CH_2Br and the CH_3 groups from the PPO (at 2.1 ppm) (Figure 3a). The functionalization ratio was fixed at 33% bromo-alkylation of PPO structural unit. The bromination was followed by ketone reduction i.e., peak i was shifted from 3 ppm to 1.7 ppm and a new peak appeared (denoted k, 2.8 ppm). The reduction of ketone groups is important because the proton in the α-position of the ketone can form enolate anions, which are strong nucleophiles and can degrade the functional groups of the membrane [49]. The ketone reduction degree (96-98%) was calculated from ^{1}H NMR spectra (Figure 3b). In the next step, the bromine alkyl side chain was reacted with

diallylmethylamine and the quaternized PPO with methyldiallylammonium was obtained (PPO-6CH_2-Q). As shown in the NMR of the PPO-6CH_2-Q (Figure 3c), where new peaks matching with the protons of diallylmethylammonium appeared.

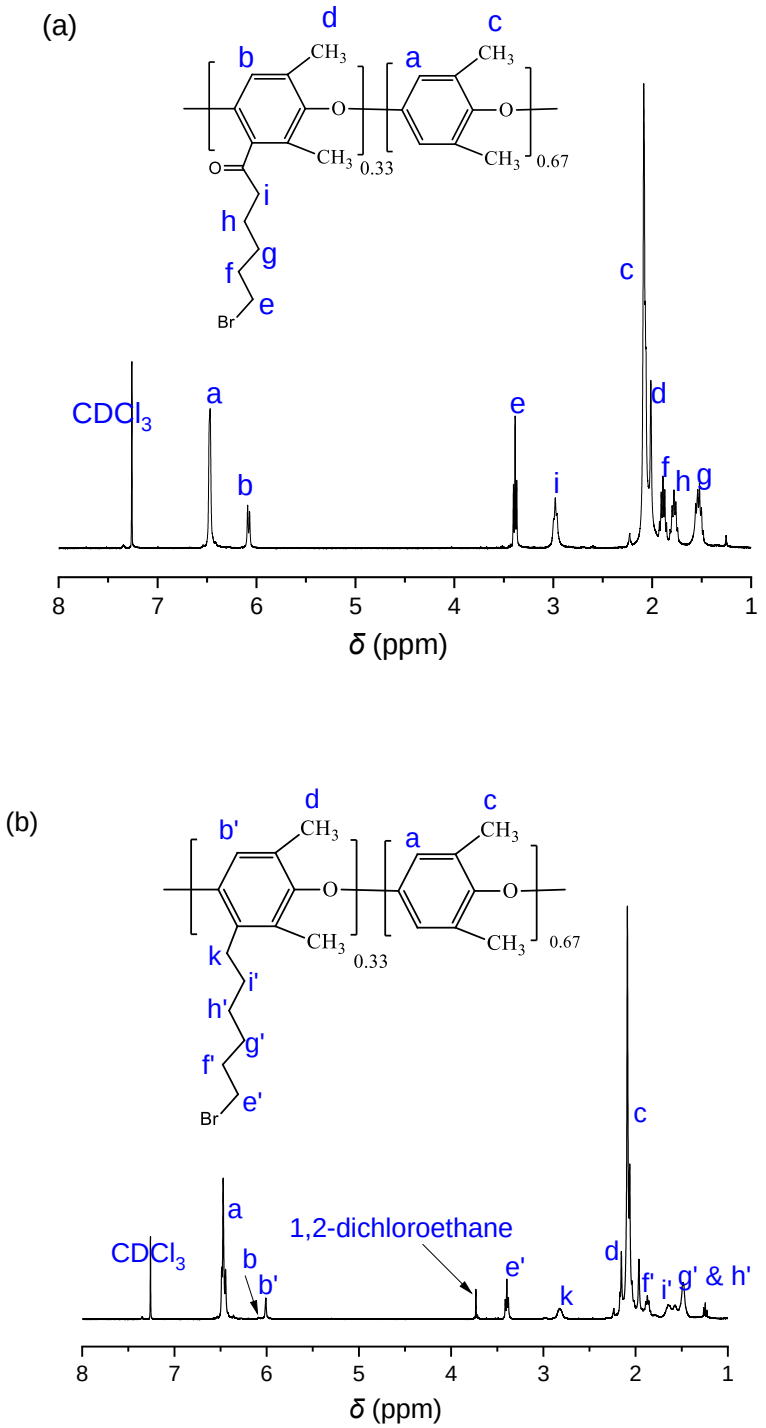

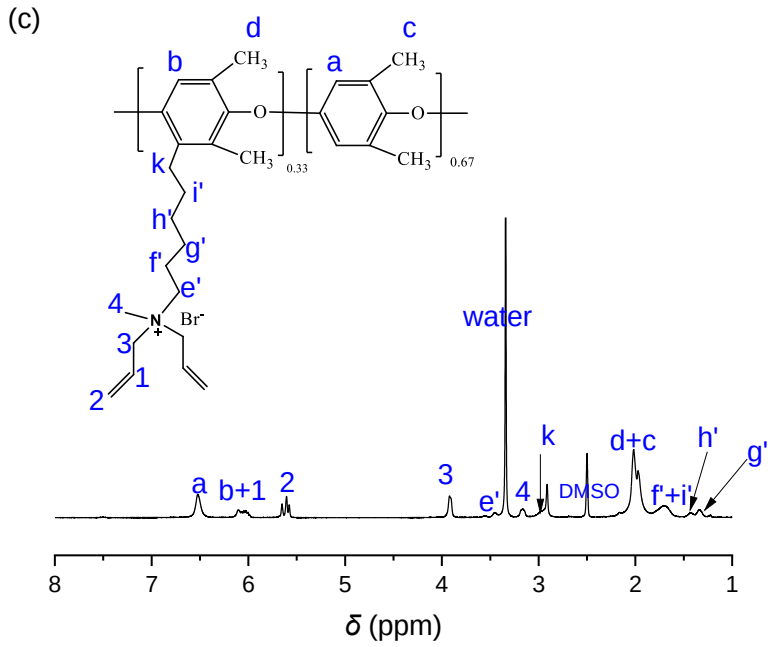

Figure 3: ^{1}H NMR spectrum of PPO-6CO-Br (a), PPO-6CH_2-Br (b) and PPO-6CH_2-Q (c).

The QA cationic monomer based on piperidine containing allyl groups, i.e., DAPCl, was synthesized in two steps following a procedure reported in the literature [39,50]. The ^{1}H NMR spectra of DAPCl is shown in Figure S1.

3.2 Ion exchange capacity

The crosslinked AEMs with thickness between 45 and 65 µm were obtained by copolymerizing PPO-6CH_2-Q with DAPCl. The ratio between PPO quaternized ammonium side chain and DAPCl was varied between 0.5 to 3 in order to prepare membranes with poly-ionic side chains, with IEC varying between 2.3 and 3.6 mmol OH^-/g. The prepared AEMs titrated IEC (Table 1) was found to vary between 2 and 3.4 mmol OH^-/g, slightly lower than the theoretical ones due to (i) incomplete polymerizations of DAPCl and (ii) the formation of poly(DAPCl), not-bonded to PPO-6CH_2-Q, which were removed from the membrane during the water washing step. Based on the titrated IEC values, the per cent (%) of DAPCl incorporated into the PPO-6CH_2-Q was calculated (DAPCl yield, Table 1). The DAPCl yield (%) increased with increasing of DAPCl to polymer ratio due to, probably, the higher number of double bonds and/or low viscosity of the

solution. It can be noted that the conversion for this class of copolymers is higher than for our previous results in which the CH_2Br was directly bonded to the PPO backbone [51].

Table 1. Thickness, IEC and DAPCl yield of the prepared membranes

AEM	Thickness (µm)	IEC (mmol Br^-/g)		IEC (mmol OH^-/g)*	$\frac{DAPCl}{PPO-6CH_2-Q}$**		DAPCl yield (%)***
		Theoretical	Titration		Feed	Titration	
PPO-6CH_2-0.5x	45 ± 3	2.00	1.80 ± 0.04	2.03 ± 0.04	0.5	0.27	53
PPO-6CH_2-1x	49 ± 3	2.26	2.03 ± 0.05	2.33 ± 0.05	1	0.59	59
PPO-6CH_2-2x	55 ± 3	2.66	2.42 ± 0.03	2.85 ± 0.03	2	1.34	67
PPO-6CH_2-3x	60 ± 3	2.91	2.80 ± 0.02	3.4 ± 0.02	3	2.52	84

*Calculated from titration IEC_{Br^-} using equation (2).

** Molar ratio of DAPCl to PPO-6CH_2-Q.

*** $\text{DAPCl yield (\%)} = \frac{\left(\frac{DAPCl}{PPO-6CH_2-Q}\right)\text{titration}}{\left(\frac{DAPCl}{PPO-6CH_2-Q}\right)\text{feed}} \times 100.$

3.3 Water uptake, ionic conductivity and surface morphology

An optimized membrane water uptake content is required for developing hydrated ionic domains as well as maintenance of membrane mechanical strength and selectivity. The water uptakes of the PPO-6CH_2-0.5x and PPO-6CH_2-3x membranes in OH^- at RT were 32 wt.% and 105 wt.%, respectively (Table 2). The increase of IEC of the membranes induces a large water-uptake because of the lengthening of the hydrophilic chains and decreases of the crosslinking density and stiffness. The water uptake of the prepared membranes is lower when compared to membranes based on PPO containing poly(DAPCl) with similar IEC, in which the allyl function was directly bonded to PPO backbone [51].

AEM with a high OH^- ion conductivity is essential for the development of high power density batteries. As the Zn slurry-air flow battery operates at RT, an AEM with high OH^- ion conductivity at RT is needed. Table 2 shows the OH^- and Cl^- (measured for comparison purpose) ions conductivities of the crosslinked AEMs. The OH^- ions conductivity of the AEMs seems to be about 2.7-4 times higher than that of their respective Cl^- ions conductivity mainly due to the difference in molar conductivities of the ions (Cl^- = 7.631 and OH^- = 19.86 mS m^2/mol), in agreement with findings reported in the literature [55].

Table 2: WU and ionic conductivity of the prepared membranes at 20 °C

Membranes	WU (OH^- form) (%)	Ionic conductivity (mS/cm)	
		Cl^-	OH^-
PPO-6CH_2-0.5x	32 (± 0.7)	0.94 (±0.15)	3.3 (± 0.2)
PPO-6CH_2-1x	55 (± 1.5)	1.9 (± 0.10)	5.2 (± 0.25)
PPO-6CH_2-2x	80 (± 3)	3.1 (± 0.2)	13 (± 0.32)
PPO-6CH_2-3x	105 (± 4)	6.6 (± 0.2)	19 (± 0.4)

As shown in Table 2, the AEMs ionic conductivity and water uptake varied significantly depending on their IEC. Generally speaking, ionic conductivity is dependent on the charge carrier concentration and their mobility. The increase in the IEC causes an increase in the amount of the charge carrier as well as their mobility. Indeed, the mobility of the charge carrier increases with an increase in water uptake. For instance, a fully hydrated PPO-6CH_2-3x membrane has a OH^- conductivity of 19 mS/cm at RT. This high value proves an efficient transportation of OH^- ion and well-connected ion channels [40], as shown in the AFM images of PPO-6CH_2-3x membrane (Figure 4).

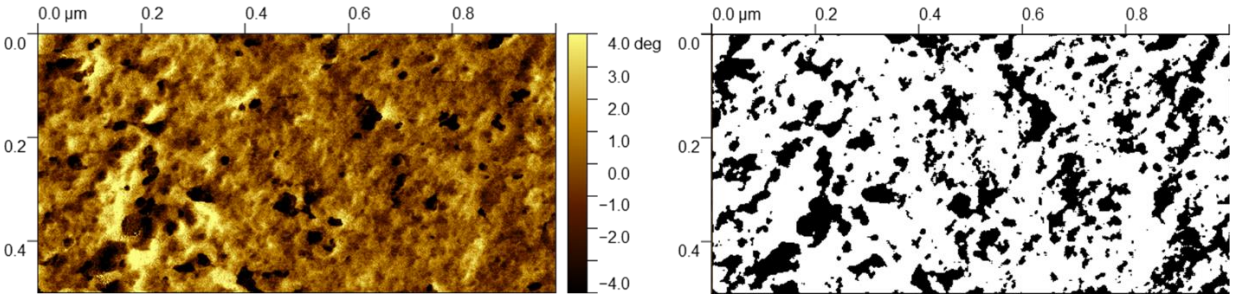

Figure 4: AFM phase image of PPO-6CH_2-3x membrane (scan size 1 µm x 0.5µm) (left) and post-treatment of AFM phase image (right); darker and lighter regions represent cationic and non-ionic groups, respectively [56].

3.4 Hydration number and water states in the membrane

The λ of the membranes was found to increase with the IEC. As shown in Table 3, PPO-6CH_2-1x membranes have approximately three more water molecules per functional group than PPO-6CH_2-0.5x membranes, with averages of 7.8 and 11.6, respectively. PPO-6CH_2-2x and PPO-6CH_2-3x, on the other hand, had higher hydration numbers, around 14 and 16.4, respectively. Similar values have been reported for other AEMs in the literature [40,57].

To determine whether the water molecules are in interaction with the ionic species or in water clusters, DSC measurements were performed. The DSC curves are given in Figure S2. There is no freezable water detected in the PPO-6CH_2-0.5x membrane, as shown in Table 3. Similarly, on the PPO-6CH_2-1x membrane, a very small amount of freezable water was detected. It can be concluded that nearly all of the water absorbed in these two membranes are in strong interaction with the ionic function [58]. Contrarily, the other two membranes, PPO-6CH_2-2x and PPO-6CH_2-3x, showed a freezable water molecule of about 2 and 6 water molecules, respectively, suggesting the presence of bulk water which are not associated with the ionic functions [59]. Overall with the exception of PPO-6CH_2-0.5x membrane, regardless of the membranes IEC and water uptake, it appears that about 11 water molecules per ionic function are in strong interaction with the polymer. Excess water molecules, on the other hand, are freely available in the membrane.

Similarly, we recently reported the amounts of freezable and non-freezable water molecules in benzylic substituted PPO-based AEMs containing *N*-spirocyclic QA cations [51]. For example, a membrane with an IEC of 2.84 mmol Cl^-/g was found to have 7 ± 0.8 freezable water molecules per ionic function.

Table 3: Water state in the AEMs: Bulky and bound water molecules

AEM	λ_{OH^-}	ΔH_f (J/g wet membrane) [a]	ΔH_f (J/g water) [b]	Bulky water (wt.%) [c]	λ in the membrane	
					Bulky	Non-freezable
PPO-6CH_2-0.5x	7.8 ± 0.3	0	0	0	0	7.8 ± 0.3
PPO-6CH_2-1x	11.6 ± 0.2	4.1 ± 0.7	11.6 ± 2	1.9 ± 0.33	0.22 ± 0.04	11.4 ± 0.1
PPO-6CH_2-2x	13.9 ± 0.5	31 ± 2.3	69.2 ± 5.1	16.6 ± 1.3	2.3 ± 0.16	11.6 ± 0.3
PPO-6CH_2-3x	16.4 ± 0.4	62 ± 3	121± 5.8	38.1 ± 1.8	6.23 ± 0.3	10.2 ± 0.4

a. Obtained from the DSC by integrating the DSC freezing curve area.

b. $\Delta H_f \left(\frac{J}{g\ water}\right) = \Delta H_f \left(\frac{J}{g\ wet\ membrane}\right) \times \frac{membrane\ weight\ (g)}{water\ weight\ in\ the\ membrane\ (g)}$

c. Freezable water (wt. %) $= \frac{\Delta H_f\left(\frac{J}{g\ water}\right)}{\Delta H_{ice,\ pure\ water}} \times Water\ uptake\ (wt.\%)$.

3.5 Zincate ions crossover

Minimizing zincate ion crossover is critical in rechargeable ZSAFB. To determine the best compromise between OH^- ion conductivity and ion selectivity, the zincate ion crossover through these AEMs was measured and compared. As shown in Figure 5, the Zn ions concentration in the depleted side increased over time for all the membranes. For e.g., for PPO-6CH_2-3x membrane, less than 5% of the Zn species crossed to the second compartment after one week.

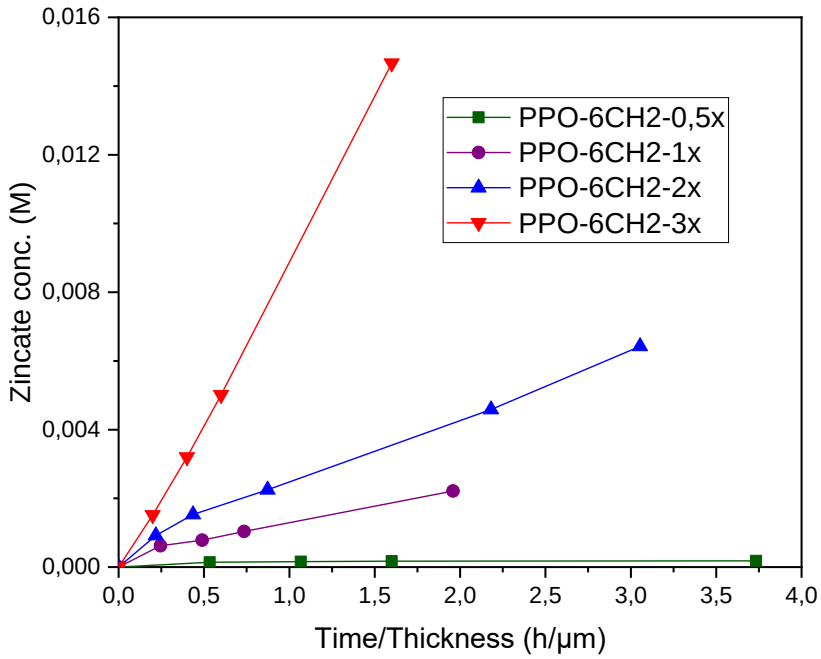

Figure 5: Plots of zincate ion crossover as a function of time/thickness. The figure lines are drawn to guide the eye.

The low D_s of zincate ion of the prepared AEMs (Table 4) could be explained by the selectivity of the ionic channels resulting from the nanophase separated morphology [28]. The membranes with higher amount of freezable or bulky water exhibited a higher $Zn(OH)_4^{2-}$ ions crossover. A larger amount of water in the ionic domains is directly related to larger ionic channel sizes and presence of free water, resulting in lower ionic species selectivity. As a result, the membranes permselectivity decreases as the IEC increases. The diffusion coefficients of zincate ions through various types of membranes, including AEMs, have been reported in the literature [19].

Table 4: Diffusion coefficient (D) of zincate ion

AEM	D (m^2/s)	Permselectivity ($S.s/m^3$)	Ref.
PPO-6CH_2-0.5x	8.9×10^{-15}	3.7×10^{13}	This study
PPO-6CH_2-1x	2.8×10^{-13}	1.9×10^{12}	
PPO-6CH_2-2x	9.7×10^{-13}	1.3×10^{12}	
PPO-6CH_2-3x	2.3×10^{-12}	8.2×10^{11}	
PPO–TMA	1.9×10^{-14}	9.2×10^{13}	[28]
AEM-Ia3¯d	1.6×10^{-13}	7.9×10^{12}	[60]
PPO-3.45 + Celgard® 3501	5.2×10^{-13}	-	[23]

3.6 Membrane stability

Long-term AEM stability in a highly alkaline solution is required for long-term use in rechargeable ZSAFBs. The PPO-6CH_2-3x (membrane with the highest IEC) was chosen as a representative sample since it is easier to correctly measure changes in ionic conductivity (and/or IEC) when membranes with high IEC are used [49].

As shown in Table 2, a fully hydrated pristine PPO-6CH_2-3x membrane has a Cl^- ion conductivity of 6.6 mS/cm at RT. The Cl^- ion conductivity of the PPO-6CH_2-3x remains constant after 14 days of immersion in both 6 M KOH (aq.) solution and Zn-slurry at RT. Moreover, the membrane maintained above 92% of its Cl^- ion conductivity after two weeks under an accelerated degradation test (1 M KOH, 60 °C). Loss in ionic conductivity of AEMs in alkaline media is mainly caused by chemical degradation of the cation and/or polymer backbone used [61]. However, it must be also noted that a minor decline in conductivity can also be caused by AEM morphology change instead of chemical degradation [62]. The mechanical flexibility and integrity of the investigated membrane seem not to be affected after the alkaline stability tests. Chemically degraded membranes are often reported to become brittle and cracked into pieces [63]. When compared to the base-stable *N*-spirocyclic-based AEMs reported in the literature, the present AEMs demonstrated comparable [39,40] or superior stability [64,65] under similar testing conditions. A comparison of *N*-spirocyclic QA-based AEMs alkaline stability is summarized in Table S1.

The high base-stability of the prepared AEMs could be due to: (i) the constrained ring conformation of the cation used inducing high transition energies for Hofmann elimination and substitution degradations [36], (ii) the grafting of the ionic side chain through a hydrophobic spacer to the polymer backbone which simultaneously removes the poor stability of PPO benzylic function [40,66] and improves the microphase

separation, making the PPO chain less susceptible to chemical attack [67] and (iii) the crosslinking, which improves the mechanical properties and limits the mobility of OH^- into the hydrophilic domain [68]. Jannasch *et al.*, [50] reported the excellent alkaline stability of poly(DAPCl) at 120 °C for 14 days.

The thermal stability of PPO-6CH_2-3x membrane was also investigated with TGA under N_2 atmosphere (Figure S3). The membrane showed two stages degradation behaviour. The first weight loss, which begins at around 300 °C is due to the heterocyclic QA groups [50], which occurs at higher temperature than that of common QA groups [40]. The last degradation which occurred at above 400 °C is ascribed to the PPO polymer backbone, and remaining Poly(DAPCl). Two stages thermal degradation of poly(DAPCl) has been reported in the literature [50].

In summary, the prepared AEMs are thermally and chemically stable enough to be employed in alkaline ZSAFB, which typically use 6 M (aq.) KOH and operate at RT.

3.7 Single ZSAFB performance

The prepared AEMs are suitable candidates for ZSAFB applications due to their high OH^- ion conductivity, alkaline stability and low zincate ion crossover. To investigate the impact of IEC of AEMs on power capability, ZSAFB single cells were built and run with the four prepared AEMs.

The cell resistances incorporating the different membranes were measured and are summarized in Figure 6(a). As expected, the IEC of the membranes, had a major impact on the cell resistance. For e.g., PPO-6CH_2-0.5x membrane–based cell exhibited the highest cell resistance (4.5 Ω cm^2) among the tested systems. Whereas, the battery using PPO-6CH_2-3x membrane displayed the lowest cell resistance, only 0.8 Ω.cm^2, despite the fact that this membrane is the thickest. Similar IEC dependency and pattern was established in the OH^- ion conductivity of the membranes. The cell resistance determined from the current density-voltage curve (Figure 6b) was about 2-3 times higher than that of cell resistances obtained through EIS measurement. This indicates the presence of additional resistance under current which may be due to the ion transport limitations.

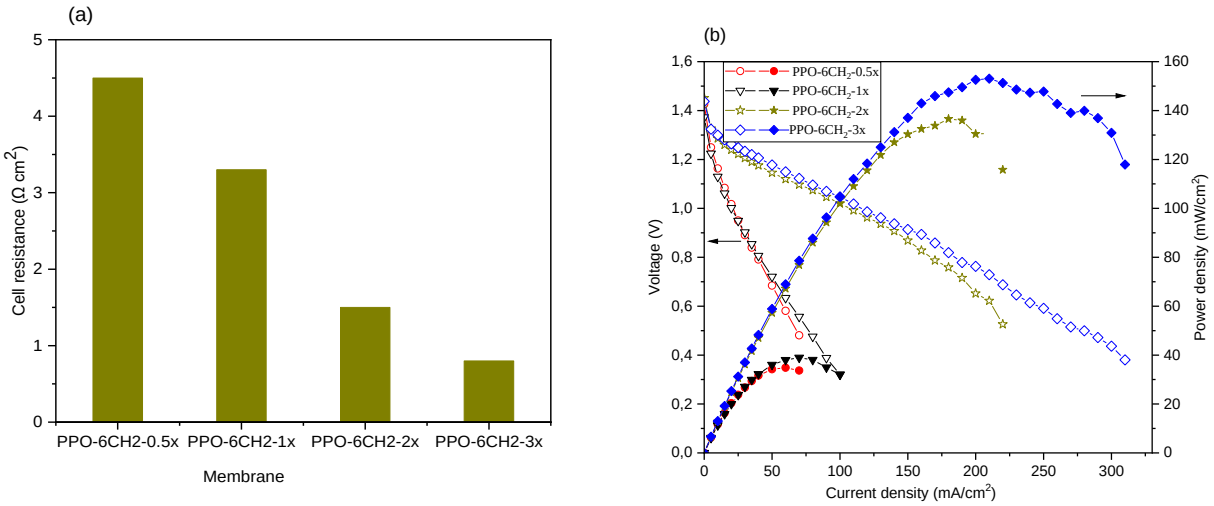

Figure 6 : Zn slurry-air flow battery (using the prepared AEMs) resistance (a) and power density (b) measured at RT, with flow rates of the Zn slurry and synthetic air of 160 and 100 mL/min, respectively.

The polarization curves are shown in Figure 6(b). All cells exhibited an OCV of about 1.4 V, showing that the AEMs are strong enough to separate the Zn-slurry electrolyte from the air electrode [68]. As predicted, both the cell voltage and the power density were found to depend on the discharge current. PPO-6CH_2-0.5x and 1x membranes delivered maximum power densities of 35 mW/cm^2 and 39 mW/cm^2, respectively. The high ohmic resistance of the membranes is detrimental for the cell, as very high current density is used. The cell assembled with PPO-6CH_2-3x membrane exhibited an excellent maximum power density (153 mW/cm^2), which is higher than that of cell assembled with PPO-6CH_2-2x (137 mW/cm^2) membrane due its higher OH^- ion conductivity. The peak power density obtained is much higher than that of the cells employing commercial porous membranes [23]. However, the cell was further optimized here, with the addition of an ionomer inside the electrode, which improves the electrochemical reaction kinetics. Furthermore, the power density attained is one of the highest values reported for Zn-air batteries employing AEMs. As summarized elsewhere [19], various Zn-air batteries employing different AEMs, such as FAA-3-based AEM (Fumatech) (9.8 mW/cm^2) [69], AEM based on poly(vinyl alcohol)/guar hydroxypropyltrimonium chloride (50 mW/cm^2) [70], QA-functionalized nanocellulose/graphene oxide AEM (44 mW/cm^2) [71], A201 tokuyama (33 mW/cm^2) [71], PPO–MPY (70 mW/cm^2) and ion-selective ionomer (PPO-3.45) coated Celgard® 3501 membrane (66 mW/cm^2) [23] have been reported to show much lower peak power densities when compared to our membranes. It should be emphasized, however, that these tests were conducted under various operating conditions. For more information on the experimental setup, including the electrolyte, electrode, and catalyst utilized, see Table S2.

It's also worth noting that the maximum power density is not the only factor to consider when selecting a membrane. Other parameters, such as the degree of zincate species crossover (i.e., closely related to capacity fade), should be evaluated as well. Overall, because the peak power densities of the single cells employing PPO-6CH_2-2x and PPO-6CH_2-3x membranes are similar, and the PPO-6CH_2-2x membrane has a much lower $Zn(OH)_4^{2-}$ ion crossover, it can be concluded that the PPO-6CH_2-2x is more promising for rechargeable ZSAFB because it is expected to have much lower capacity fade during cyclability testing. The peak power density and $Zn(OH)_4^{2-}$ ion crossover tradeoff are shown in Figure 7. The cyclability of the developed system will be investigated in future works.

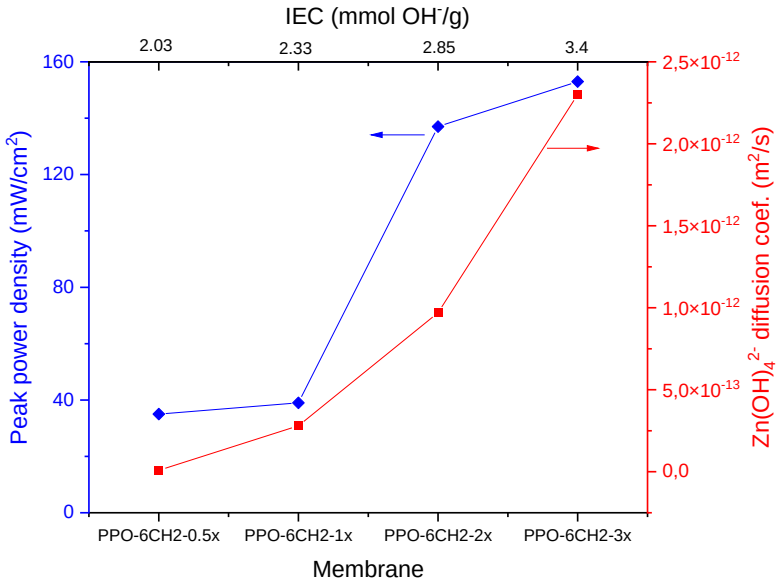

Figure 7: The impact of membrane IEC on peak power density and $Zn(OH)_4^{2-}$ ion crossover.

4. Conclusion

Here, we have successfully prepared four AEMs, in which the multi *N*-spirocyclic QAs were grafted to the PPO polymer backbone with 6-C spacer through UV-irradiation. The IEC of each AEM was

controlled by changing the ratio between DAPCl and PPO-6CH_2-Q. AFM analysis clearly showed well-defined phase separation in PPO-6CH_2-3x membrane, which results in excellent OH^- ion conductivity at room temperature. The membranes displayed an excellent alkaline stability in 1 M KOH at 60 °C, with less than 8% drop in ionic conductivity after 360 h of the stability test. Furthermore, the membranes showed no signs of chemical degradation in a typical electrolyte used in ZSAFBs. The OH^- ion conductivity, amount of bulky or freezable water, permselectivity and battery performances of the AEMs were mostly influenced by the IEC of the AEMs. AEMs with low IECs, and thus little or no freezable water molecules exhibited negligible zincate ion crossover, whereas AEMs with high IECs (freezable water molecules) had much higher zincate ion crossover, implying that bulky water may play a role in increasing unwanted zincate ion crossover. Even though the IEC sacrifices the zincate ion selectivity of the AEMs, however, it merits the peak power densities of the ZSAFBs. A single ZSAFB with PPO-6CH_2-3x delivered a maximum power density of 153 mW/cm^2. On the other hand, given its low zincate ion crossover and high power density (137 mW/cm^2), the PPO-6CH_2-2x is a very promising membrane for alkaline batteries, including rechargeable ZSAFB. In future research, we believe it is vital to look into the long-term durability of the membranes in a ZSAFB and their mechanical strengths.

Supporting information

^{1}H NMR spectrum of *N*-allylpiperidine in $CDCl_3$ and of *N*,*N*-diallylpiperidinum chloride (DAPCl) in H_2O, DSC curves of PPO-6CH_2-0.5x, PPO-6CH_2-1x, PPO-6CH_2-2x and PPO-6CH_2-3x membranes, TGA curves of PPO-6CH_2-3x membrane, comparison of alkaline stability of selected *N*-spirocyclic quaternary ammonium-based AEMs and Anion exchange membranes used in Zn-air batteries.

Funding: This project has received funding from the European Union's Horizon 2020 research and innovation programme under the Marie Skłodowska-Curie Grant Agreement no. 765289. This work was performed within the framework of the Centre of Excellence of Multifunctional Architectured Materials "CEMAM" no. AN-10-LABX-44-01

References

(1) Winsberg, J.; Hagemann, T.; Janoschka, T.; Hager, M. D.; Schubert, U. S. Redox-Flow Batteries: From Metals to Organic Redox-Active Materials. *Angew. Chemie Int. Ed.* **2017**, *56* (3), 686–711. https://doi.org/10.1002/anie.201604925.

(2) Yang, Z.; Zhang, J.; Kintner-Meyer, M. C. W.; Lu, X.; Choi, D.; Lemmon, J. P.; Liu, J. Electrochemical Energy Storage for Green Grid. *Chemical Reviews*. American Chemical Society May 11, 2011, pp 3577–3613. https://doi.org/10.1021/cr100290v.

(3) Dunn, B.; Kamath, H.; Tarascon, J. M. Electrical Energy Storage for the Grid: A Battery of

Choices. *Science*. American Association for the Advancement of Science November 18, 2011, pp 928–935. https://doi.org/10.1126/science.1212741.

(4) Skyllas-Kazacos, M.; Chakrabarti, M. H.; Hajimolana, S. A.; Mjalli, F. S.; Saleem, M. Progress in Flow Battery Research and Development. *J. Electrochem. Soc.* **2011**, *158* (8), R55. https://doi.org/10.1149/1.3599565.

(5) Amrouche, S. O.; Rekioua, D.; Rekioua, T.; Bacha, S. Overview of Energy Storage in Renewable Energy Systems. **2016**. https://doi.org/10.1016/j.ijhydene.2016.06.243.

(6) Nitta, N.; Wu, F.; Lee, J. T.; Yushin, G. Li-Ion Battery Materials: Present and Future. *Mater. Today* **2015**, *18* (5). https://doi.org/10.1016/j.mattod.2014.10.040.

(7) Abdin, Z.; Khalilpour, K. R. Single and Polystorage Technologies for Renewable-Based Hybrid Energy Systems. In *Polygeneration with Polystorage: For Chemical and Energy Hubs*; Elsevier, 2018; pp 77–131. https://doi.org/10.1016/B978-0-12-813306-4.00004-5.

(8) Johnson, S. C.; Todd Davidson, F.; Rhodes, J. D.; Coleman, J. L.; Bragg-Sitton, S. M.; Dufek, E. J.; Webber, M. E. Selecting Favorable Energy Storage Technologies for Nuclear Power. In *Storage and Hybridization of Nuclear Energy: Techno-economic Integration of Renewable and Nuclear Energy*; Elsevier, 2018; pp 119–175. https://doi.org/10.1016/B978-0-12-813975-2.00005-3.

(9) Wu, X.; Song, K.; Zhang, X.; Hu, N.; Li, L.; Li, W.; Zhang, L.; Zhang, H. Safety Issues in Lithium Ion Batteries: Materials and Cell Design. *Frontiers in Energy Research*. Frontiers Media S.A. July 17, 2019, p 65. https://doi.org/10.3389/fenrg.2019.00065.

(10) Matte, T. D.; Figueroa, J. P.; Burr, G.; Flesch, J. P.; Keenlyside, R. A.; Baker, E. L. Lead Exposure among Lead-Acid Battery Workers in Jamaica. *Am. J. Ind. Med.* **1989**, *16* (2), 167–177. https://doi.org/10.1002/ajim.4700160208.

(11) Van Der Kuijp, T. J.; Huang, L.; Cherry, C. R. Health Hazards of China's Lead-Acid Battery Industry: A Review of Its Market Drivers, Production Processes, and Health Impacts. *Environmental Health: A Global Access Science Source*. BioMed Central August 3, 2013, pp 1–10. https://doi.org/10.1186/1476-069X-12-61.

(12) Whyte, I. A. N.; Limited, P. R. Flow Battery Design, Scale-up, and Manufacture; 2018.

(13) Yang, Z. G. Status and Future Perspectives of Redox Flow Batteries; 2018.

(14) Colli, A. N.; Peljo, P.; Girault, H. H. High Energy Density MnO4-/MnO42- Redox Couple for Alkaline Redox Flow Batteries. *Chem. Commun.* **2016**, *52* (97), 14039–14042. https://doi.org/10.1039/c6cc08070g.

(15) Roe, S.; Menictas, C.; Skyllas-Kazacos, M. A High Energy Density Vanadium Redox Flow Battery with 3 M Vanadium Electrolyte. *J. Electrochem. Soc.* **2016**, *163* (1), A5023–A5028. https://doi.org/10.1149/2.0041601jes.

(16) Caramia, V.; Bozzini, B. Materials Science Aspects of Zinc–Air Batteries: A Review. *Mater.*

Renew. Sustain. Energy **2014**, *3* (2), 28. https://doi.org/10.1007/s40243-014-0028-3.

(17) Choi, N.; del Olmo, D.; Fischer, P.; Pinkwart, K.; Tübke, J. Development of Flow Fields for Zinc Slurry Air Flow Batteries. *Batteries* **2020**, *6* (1), 15. https://doi.org/10.3390/batteries6010015.

(18) Tsehaye, M. T.; Alloin, F.; Iojoiu, C. Prospects for Anion-Exchange Membranes in Alkali Metal–Air Batteries. *Energies* **2019**, *12* (24), 4702. https://doi.org/10.3390/en12244702.

(19) Tsehaye, M. T.; Alloin, F.; Iojoiu, C.; Tufa, R. A.; Aili, D.; Fischer, P.; Velizarov, S. Membranes for Zinc-Air Batteries: Recent Progress, Challenges and Perspectives. *J. Power Sources* **2020**, *475*, 228689. https://doi.org/10.1016/j.jpowsour.2020.228689.

(20) Lee, H.-J.; Lim, J.-M.; Kim, H.-W.; Jeong, S.-H.; Eom, S.-W.; Hong, Y. T.; Lee, S.-Y. Electrospun Polyetherimide Nanofiber Mat-Reinforced, Permselective Polyvinyl Alcohol Composite Separator Membranes: A Membrane-Driven Step Closer toward Rechargeable Zinc–Air Batteries. *J. Memb. Sci.* **2016**, *499*, 526–537. https://doi.org/10.1016/j.memsci.2015.10.038.

(21) Hwang, H. J.; Chi, W. S.; Kwon, O.; Lee, J. G.; Kim, J. H.; Shul, Y.-G. Selective Ion Transporting Polymerized Ionic Liquid Membrane Separator for Enhancing Cycle Stability and Durability in Secondary Zinc–Air Battery Systems. *ACS Appl. Mater. Interfaces* **2016**, *8* (39), 26298–26308. https://doi.org/10.1021/acsami.6b07841.

(22) Krejčí, I.; Vanýsek, P.; Trojánek, A. Transport of Zn (OH) 4 2 − Ions across a Polyolefin Microporous Membrane. *J. Electrochem. Soc.* **1993**, *140* (8), 2279–2283. https://doi.org/10.1149/1.2220808.

(23) Tsehaye, M. T.; Teklay Gebreslassie, G.; Heon Choi, N.; Milian, D.; Martin, V.; Fischer, P.; Tübke, J.; El Kissi, N.; Donten, M. L.; Alloin, F.; Iojoiu, C. Pristine and Modified Porous Membranes for Zinc Slurry–Air Flow Battery. *Molecules* **2021**, *26* (13), 4062. https://doi.org/10.3390/molecules26134062.

(24) Kiros, Y. Separation and Permeability of Zincate Ions through Membranes. *J. Power Sources* **1996**, *62* (1), 117–119. https://doi.org/10.1016/S0378-7753(96)02420-2.

(25) Fu, J.; Cano, Z. P.; Park, M. G.; Yu, A.; Fowler, M.; Chen, Z. Electrically Rechargeable Zinc-Air Batteries: Progress, Challenges, and Perspectives. *Adv. Mater.* **2017**, *29* (7), 1604685. https://doi.org/10.1002/adma.201604685.

(26) Li, Y.; Dai, H. Recent Advances in Zinc–Air Batteries. *Chem. Soc. Rev.* **2014**, *43* (15), 5257–5275. https://doi.org/10.1039/C4CS00015C.

(27) Dewi, E. L.; Oyaizu, K.; Nishide, H.; Tsuchida, E. Cationic Polysulfonium Membrane as Separator in Zinc–Air Cell. *J. Power Sources* **2003**, *115* (1), 149–152. https://doi.org/10.1016/S0378-7753(02)00650-X.

(28) Abbasi, A.; Hosseini, S.; Somwangthanaroj, A.; Mohamad, A. A.; Kheawhom, S. Poly(2,6-Dimethyl-1,4-Phenylene Oxide)-Based Hydroxide Exchange Separator Membranes for Zinc–

Air Battery. *Int. J. Mol. Sci.* **2019**, *20* (15), 3678. https://doi.org/10.3390/ijms20153678.

(29) Fu, J.; Zhang, J.; Song, X.; Zarrin, H.; Tian, X.; Qiao, J.; Rasen, L.; Li, K.; Chen, Z. A Flexible Solid-State Electrolyte for Wide-Scale Integration of Rechargeable Zinc-Air Batteries. *Energy Environ. Sci.* **2016**, *9* (2), 663–670. https://doi.org/10.1039/c5ee03404c.

(30) Zhang, J.; Fu, J.; Song, X.; Jiang, G.; Zarrin, H.; Xu, P.; Li, K.; Yu, A.; Chen, Z. Laminated Cross-Linked Nanocellulose/Graphene Oxide Electrolyte for Flexible Rechargeable Zinc-Air Batteries. *Adv. Energy Mater.* **2016**, *6* (14), 1600476. https://doi.org/10.1002/aenm.201600476.

(31) Kwon, O.; Hwang, H. J.; Ji, Y.; Jeon, O. S.; Kim, J. P.; Lee, C.; Shul, Y. G. Transparent Bendable Secondary Zinc-Air Batteries by Controlled Void Ionic Separators. *Sci. Rep.* **2019**, *9* (1), 1–9. https://doi.org/10.1038/s41598-019-38552-4.

(32) Soni, R.; Bhange, S. N.; Kurungot, S. A 3-D Nanoribbon-like Pt-Free Oxygen Reduction Reaction Electrocatalyst Derived from Waste Leather for Anion Exchange Membrane Fuel Cells and Zinc-Air Batteries. *Nanoscale* **2019**, *11* (16), 7893–7902. https://doi.org/10.1039/c9nr00977a.

(33) Zhang, F.; Zhang, H.; Qu, C. Imidazolium Functionalized Polysulfone Anion Exchange Membrane for Fuel Cell Application. *J. Mater. Chem.* **2011**, *21* (34), 12744. https://doi.org/10.1039/c1jm10656b.

(34) Varcoe, J. R.; Atanassov, P.; Dekel, D. R.; Herring, A. M.; Hickner, M. A.; Kohl, P. A.; Kucernak, A. R.; Mustain, W. E.; Nijmeijer, K.; Scott, K.; Xu, T.; Zhuang, L. Anion-Exchange Membranes in Electrochemical Energy Systems. *Energy Environ. Sci.* **2014**, *7* (10), 3135–3191. https://doi.org/10.1039/C4EE01303D.

(35) Yang, Z.; Zhou, J.; Wang, S.; Hou, J.; Wu, L.; Xu, T. A Strategy to Construct Alkali-Stable Anion Exchange Membranes Bearing Ammonium Groups via Flexible Spacers. *J. Mater. Chem. A* **2015**, *3* (29), 15015–15019. https://doi.org/10.1039/C5TA02941D.

(36) Marino, M. G.; Kreuer, K. D. Alkaline Stability of Quaternary Ammonium Cations for Alkaline Fuel Cell Membranes and Ionic Liquids. *ChemSusChem* **2015**, *8* (3), 513–523. https://doi.org/10.1002/cssc.201403022.

(37) Olsson, J. S.; Pham, T. H.; Jannasch, P. Poly(Arylene Piperidinium) Hydroxide Ion Exchange Membranes: Synthesis, Alkaline Stability, and Conductivity. *Adv. Funct. Mater.* **2018**, *28* (2), 1702758. https://doi.org/10.1002/adfm.201702758.

(38) Pham, T. H.; Olsson, J. S.; Jannasch, P. Poly(Arylene Alkylene)s with Pendant N -Spirocyclic Quaternary Ammonium Cations for Anion Exchange Membranes. *J. Mater. Chem. A* **2018**, *6* (34), 16537–16547. https://doi.org/10.1039/C8TA04699A.

(39) Strasser, D. J.; Graziano, B. J.; Knauss, D. M. Base Stable Poly(Diallylpiperidinium Hydroxide) Multiblock Copolymers for Anion Exchange Membranes. *J. Mater. Chem. A* **2017**, *5* (20), 9627–9640. https://doi.org/10.1039/C7TA00905D.

(40) Xue, J.; Liu, X.; Zhang, J.; Yin, Y.; Guiver, M. D. Poly(Phenylene Oxide)s Incorporating N-Spirocyclic Quaternary Ammonium Cation/Cation Strings for Anion Exchange Membranes. *J. Memb. Sci.* **2020**, *595*, 117507. https://doi.org/10.1016/j.memsci.2019.117507.

(41) Nuñez, S. A.; Hickner, M. A. Quantitative 1 H NMR Analysis of Chemical Stabilities in Anion-Exchange Membranes. *ACS Macro Lett.* **2013**, *2* (1), 49–52. https://doi.org/10.1021/mz300486h.

(42) Li, N.; Leng, Y.; Hickner, M. A.; Wang, C.-Y. Highly Stable, Anion Conductive, Comb-Shaped Copolymers for Alkaline Fuel Cells. *J. Am. Chem. Soc.* **2013**, *135* (27), 10124–10133. https://doi.org/10.1021/ja403671u.

(43) Dang, H.-S.; Jannasch, P. Exploring Different Cationic Alkyl Side Chain Designs for Enhanced Alkaline Stability and Hydroxide Ion Conductivity of Anion-Exchange Membranes. *Macromolecules* **2015**, *48* (16), 5742–5751. https://doi.org/10.1021/acs.macromol.5b01302.

(44) Xu, T.; Wu, D.; Wu, L. Poly(2,6-Dimethyl-1,4-Phenylene Oxide) (PPO)—A Versatile Starting Polymer for Proton Conductive Membranes (PCMs). *Prog. Polym. Sci.* **2008**, *33* (9), 894–915. https://doi.org/10.1016/j.progpolymsci.2008.07.002.

(45) Ran, J.; Wu, L.; Ru, Y.; Hu, M.; Din, L.; Xu, T. Anion Exchange Membranes (AEMs) Based on Poly(2,6-Dimethyl-1,4-Phenylene Oxide) (PPO) and Its Derivatives. *Polym. Chem.* **2015**, *6* (32), 5809–5826. https://doi.org/10.1039/C4PY01671H.

(46) Pham, T. H.; Jannasch, P. Aromatic Polymers Incorporating Bis- N -Spirocyclic Quaternary Ammonium Moieties for Anion-Exchange Membranes. *ACS Macro Lett.* **2015**, *4* (12), 1370–1375. https://doi.org/10.1021/acsmacrolett.5b00690.

(47) Cheng, C.; He, X.; Huang, S.; Zhang, F.; Guo, Y.; Wen, Y.; Wu, B.; Chen, D. Novel Self-Cross-Linked Multi-Imidazolium Cations Long Flexible Side Chains Triblock Copolymer Anion Exchange Membrane Based on ROMP-Type Polybenzonorbornadiene. *Int. J. Hydrogen Energy* **2020**, *45* (38), 19676–19690. https://doi.org/10.1016/j.ijhydene.2020.04.276.

(48) Hibbs, M. R. Alkaline Stability of Poly(Phenylene)-Based Anion Exchange Membranes with Various Cations. *J. Polym. Sci. Part B Polym. Phys.* **2013**, *51* (24), 1736–1742. https://doi.org/10.1002/polb.23149.

(49) Parrondo, J.; Jung, M. J.; Wang, Z.; Arges, C. G.; Ramani, V. Synthesis and Alkaline Stability of Solubilized Anion Exchange Membrane Binders Based on Poly(Phenylene Oxide) Functionalized with Quaternary Ammonium Groups via a Hexyl Spacer. *J. Electrochem. Soc.* **2015**, *162* (10), F1236–F1242. https://doi.org/10.1149/2.0891510jes.

(50) Olsson, J. S.; Pham, T. H.; Jannasch, P. Poly(N , N -Diallylazacycloalkane)s for Anion-Exchange Membranes Functionalized with N -Spirocyclic Quaternary Ammonium Cations. *Macromolecules* **2017**, *50* (7), 2784–2793. https://doi.org/10.1021/acs.macromol.7b00168.

(51) Tsehaye, M.; Yang, X.; Janoschka, T.; Hager, M.; Schubert, U.; Alloin, F.; Iojoiu, C. Study of

Anion Exchange Membrane Properties Incorporating N-Spirocyclic Quaternary Ammonium Cations and Aqueous Organic Redox Flow Battery Performance. *Membranes (Basel).* **2021**, *11* (5), 367. https://doi.org/10.3390/membranes11050367.

(52) James, P. J.; Antognozzi, M.; Tamayo, J.; McMaster, T. J.; Newton, J. M.; Miles, M. J. Interpretation of Contrast in Tapping Mode AFM and Shear Force Microscopy. A Study of Nafion. *Langmuir* **2001**. https://doi.org/10.1021/la000332h.

(53) Kim, H.-W.; Lim, J.-M.; Lee, H.-J.; Eom, S.-W.; Hong, Y. T.; Lee, S.-Y. Artificially Engineered, Bicontinuous Anion-Conducting/-Repelling Polymeric Phases as a Selective Ion Transport Channel for Rechargeable Zinc–Air Battery Separator Membranes. *J. Mater. Chem. A* **2016**, *4* (10), 3711–3720. https://doi.org/10.1039/C5TA09576J.

(54) Choi, N. H.; Del Olmo, D.; Fischer, P.; Pinkwart, K.; Tübke, J. Development of Flow Fields for Zinc Slurry Air Flow Batteries. *Batteries* **2020**, *6* (1), 1–10. https://doi.org/10.3390/batteries6010015.

(55) Hou, J.; Liu, Y.; Ge, Q.; Yang, Z.; Wu, L.; Xu, T. Recyclable Cross-Linked Anion Exchange Membrane for Alkaline Fuel Cell Application. *J. Power Sources* **2018**, *375*, 404–411. https://doi.org/10.1016/j.jpowsour.2017.06.073.

(56) Badami, A. S.; Lane, O.; Lee, H. S.; Roy, A.; McGrath, J. E. Fundamental Investigations of the Effect of the Linkage Group on the Behavior of Hydrophilic-Hydrophobic Poly(Arylene Ether Sulfone) Multiblock Copolymers for Proton Exchange Membrane Fuel Cells. *J. Memb. Sci.* **2009**. https://doi.org/10.1016/j.memsci.2008.12.066.

(57) Weiber, E. A.; Jannasch, P. Ion Distribution in Quaternary-Ammonium-Functionalized Aromatic Polymers: Effects on the Ionic Clustering and Conductivity of Anion-Exchange Membranes. *ChemSusChem* **2014**, *7* (9), 2621–2630. https://doi.org/10.1002/cssc.201402223.

(58) Liu, L.; Huang, G.; Kohl, P. A. Anion Conducting Multiblock Copolymers with Multiple Head-Groups. *J. Mater. Chem. A* **2018**, *6* (19), 9000–9008. https://doi.org/10.1039/C8TA00753E.

(59) Lue, S. J.; Shieh, S.-J. Water States in Perfluorosulfonic Acid Membranes Using Differential Scanning Calorimetry. *J. Macromol. Sci. Part B* **2009**, *48* (1), 114–127. https://doi.org/10.1080/00222340802561649.

(60) Sun, N.; Lu, F.; Mariani, A.; Passerini, S.; Gao, X.; Zheng, L. Anion Exchange Membrane Electrolyte Preserving Inverse Ia3¯d Bicontinuous Cubic Phase: Effect of Microdomain Morphology on Selective Ion Transport. *J. Memb. Sci.* **2020**, *605*, 118113. https://doi.org/10.1016/j.memsci.2020.118113.

(61) Wang, X. Q.; Lin, C. X.; Liu, F. H.; Li, L.; Yang, Q.; Zhang, Q. G.; Zhu, A. M.; Liu, Q. L. Alkali-Stable Partially Fluorinated Poly(Arylene Ether) Anion Exchange Membranes with a Claw-Type Head for Fuel Cells. *J. Mater. Chem. A* **2018**, *6* (26), 12455–12465. https://doi.org/10.1039/C8TA03437K.

(62) Dang, H.-S.; Jannasch, P. Alkali-Stable and Highly Anion Conducting Poly(Phenylene Oxide)s Carrying Quaternary Piperidinium Cations. *J. Mater. Chem. A* **2016**, *4* (30), 11924–11938. https://doi.org/10.1039/C6TA01905F.

(63) You, W.; Padgett, E.; MacMillan, S. N.; Muller, D. A.; Coates, G. W. Highly Conductive and Chemically Stable Alkaline Anion Exchange Membranes via ROMP of Trans -Cyclooctene Derivatives. *Proc. Natl. Acad. Sci.* **2019**, *116* (20), 9729–9734. https://doi.org/10.1073/pnas.1900988116.

(64) Shen, B.; Sana, B.; Pu, H. Multi-Block Poly(Ether Sulfone) for Anion Exchange Membranes with Long Side Chains Densely Terminated by Piperidinium. *J. Memb. Sci.* **2020**, *615*, 118537. https://doi.org/10.1016/j.memsci.2020.118537.

(65) Shang, L.; Yao, D.; Pang, B.; Zhao, C. Anion Exchange Membranes Based on Poly (Ether Ether Ketone) Containing N-Spirocyclic Quaternary Ammonium Cations in Phenyl Side Chain. *Int. J. Hydrogen Energy* **2021**, *46* (36), 19116–19128. https://doi.org/10.1016/j.ijhydene.2021.03.059.

(66) Dang, H. S.; Jannasch, P. A Comparative Study of Anion-Exchange Membranes Tethered with Different Hetero-Cycloaliphatic Quaternary Ammonium Hydroxides. *J. Mater. Chem. A* **2017**, *5* (41), 21965–21978. https://doi.org/10.1039/C7TA06029G.

(67) Shin, D. W.; Guiver, M. D.; Lee, Y. M. Hydrocarbon-Based Polymer Electrolyte Membranes: Importance of Morphology on Ion Transport and Membrane Stability. *Chem. Rev.* **2017**, *117* (6), 4759–4805. https://doi.org/10.1021/acs.chemrev.6b00586.

(68) Zhang, Y.; Chen, W.; Yan, X.; Zhang, F.; Wang, X.; Wu, X.; Pang, B.; Wang, J.; He, G. Ether Spaced N-Spirocyclic Quaternary Ammonium Functionalized Crosslinked Polysulfone for High Alkaline Stable Anion Exchange Membranes. *J. Memb. Sci.* **2020**, *598*, 117650. https://doi.org/10.1016/j.memsci.2019.117650.

(69) Kwon, O.; Hwang, H. J.; Ji, Y.; Jeon, O. S.; Kim, J. P.; Lee, C.; Shul, Y. G. Transparent Bendable Secondary Zinc-Air Batteries by Controlled Void Ionic Separators. *Sci. Rep.* **2019**, *9* (1), 3175. https://doi.org/10.1038/s41598-019-38552-4.

(70) Wang, M.; Xu, N.; Fu, J.; Liu, Y.; Qiao, J. High-Performance Binary Cross-Linked Alkaline Anion Polymer Electrolyte Membranes for All-Solid-State Supercapacitors and Flexible Rechargeable Zinc–Air Batteries. *J. Mater. Chem. A* **2019**, *7* (18), 11257–11264. https://doi.org/10.1039/C9TA02314C.

(71) Zhang, J.; Fu, J.; Song, X.; Jiang, G.; Zarrin, H.; Xu, P.; Li, K.; Yu, A.; Chen, Z. Laminated Cross-Linked Nanocellulose/Graphene Oxide Electrolyte for Flexible Rechargeable Zinc-Air Batteries. *Adv. Energy Mater.* **2016**, *6* (14), 1600476. https://doi.org/10.1002/aenm.201600476.

Electronic Supplementary Information (ESI)

Anion exchange membranes incorporating multi *N*-spirocyclic quaternary ammonium cations *via* UV-initiated polymerization for zinc slurry-air flow batteries

Misgina Tilahun Tsehaye[a], Nak Heon Choi[b,c], Peter Fischer[b], Jens Tübke[b,c], Emilie Planes[a], Fannie Alloin[a]*, Cristina Iojoiu[a]*

[a] Univ. Grenoble Alpes, Univ. Savoie Mont Blanc, CNRS, Grenoble INP, LEPMI, 38 000 Grenoble, France

[b]Applied Electrochemistry, Fraunhofer Institute for Chemical Technology ICT, Joseph-von-Fraunhofer, Straße 7, 76327 Pfinztal, Germany

[c]Institute for Mechanical Process Engineering and Mechanics, Karlsruhe Institute of Technology KIT, Straße am Forum 8, 76131 Karlsruhe, Germany

Corresponding authors*: Fannie.Alloin@lepmi.grenoble-inp.fr Cristina.iojoiu@lepmi.grenoble-inp.fr

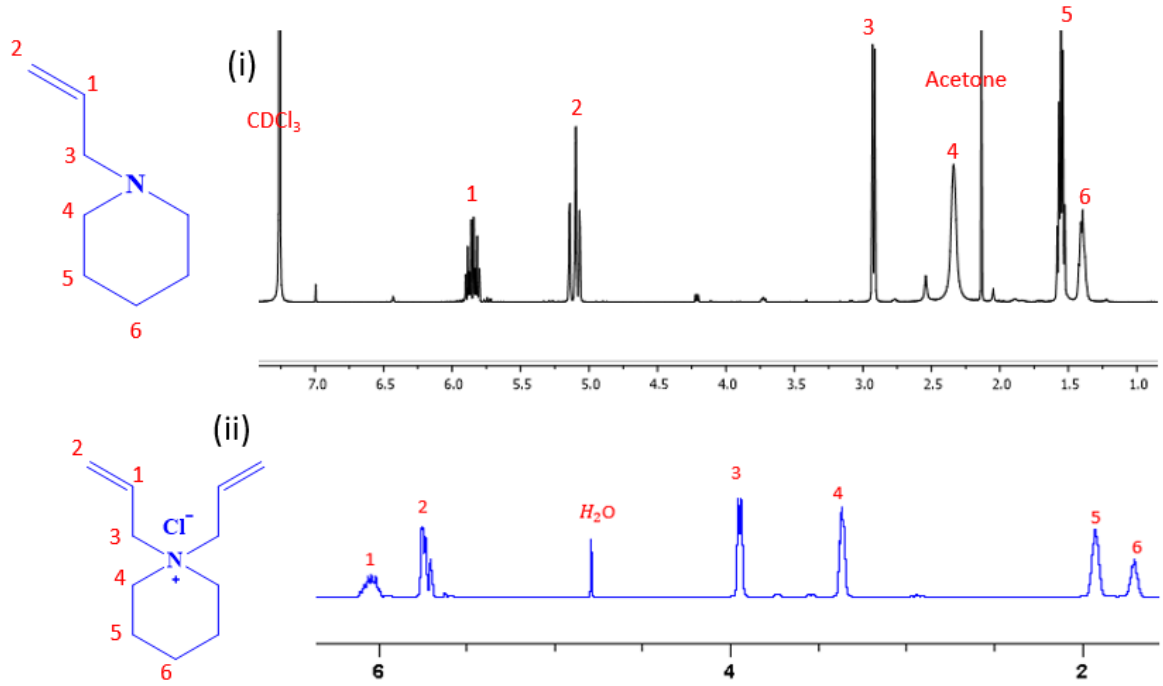

Figure S1: ^{1}H NMR spectrum of (i) *N*-allylpiperidine in $CDCl_3$ and of (ii) *N*,*N*-diallylpiperidinum chloride (DAPCl) in H_2O.

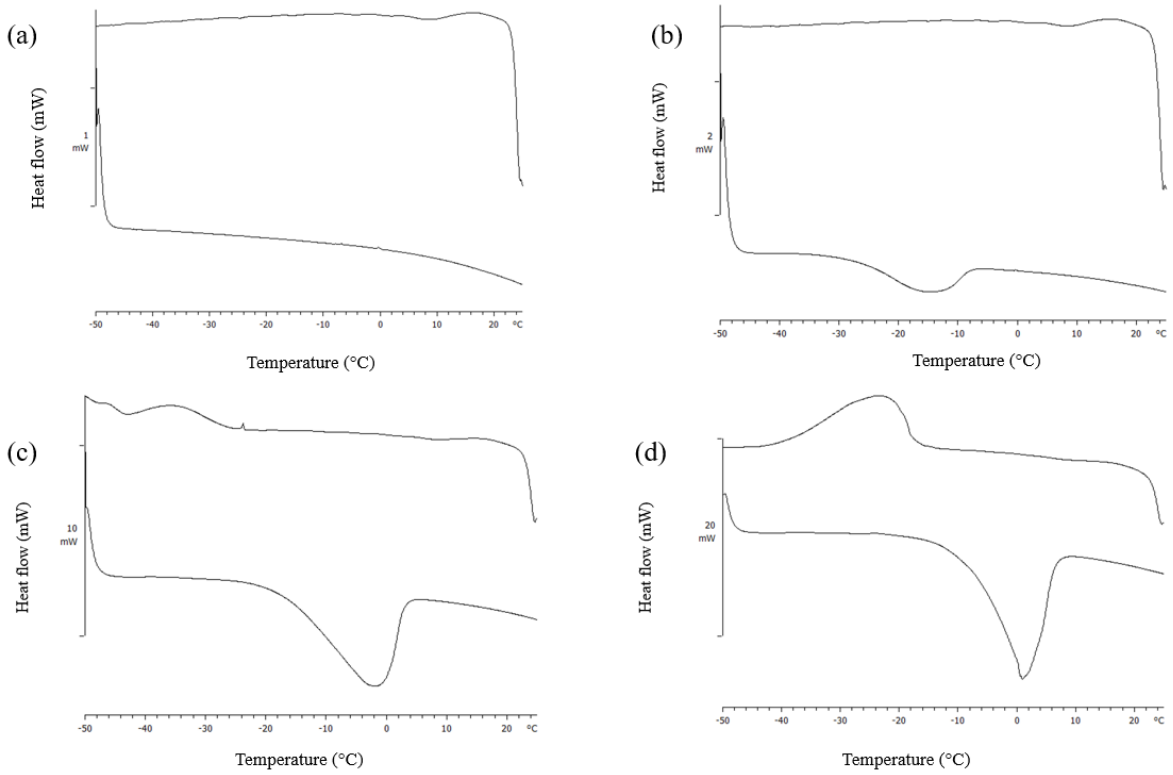

Figure S2: DSC curves of (a) PPO-6CH_2-0.5x, (b) PPO-6CH_2-1x, (c) PPO-6CH_2-2x and (d) PPO-6CH_2-3x membranes.

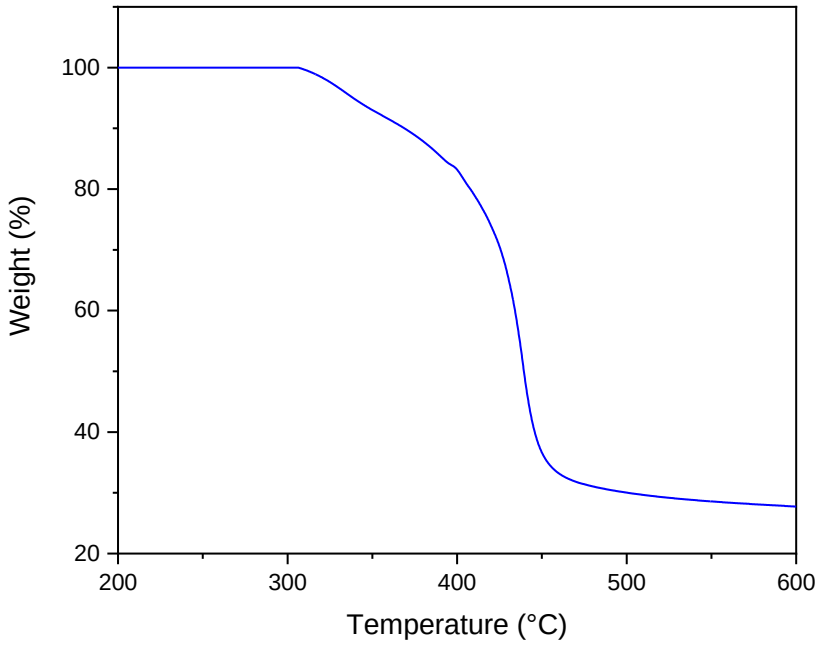

Figure S3: TGA curves of PPO-6CH_2-3x membrane.

Table S1: Comparison of alkaline stability of selected *N*-spirocyclic quaternary ammonium-based AEMs.

Membrane	**Cation**	**Test conditions: Concentration, temperature and duration**	**Alkaline stability: Retention in σ and/or IEC***	**Ref.**
PSf–PDApip3	ASD	1 M KOH at 80 °C,120 h	94% (σ)	[1]
PBP-ASU-PPO	ASU	1 M NaOH at 80 °C, 2000 h	86.4% (σ)	[2]
Cr-ASU-PSF 1.92	ASU	1 M KOH at 80 °C, 720 h	95.6% (σ)	[3]
PPO-SDSU-36	DSU	1 M aq NaOH at 80 °C, 360 h	67% (σ) and 63% (IEC).	[4]
PB-ASU	ASU	3 M $NaOH_{aq}$ at 80 °C, 2000 h	94.5% (σ)	[5]
PPO-ASU-40	ASU	10 M NaOH at 80 °C, 250 h	53.8% (σ)	[6]
ASU-PPO	ASU	1 M NaOH(aq) at 80 °C, 720 h	96.7% (σ)	[7]
[PAPi][OH]	ASU	1 M NaOH 80 °C, 168 h	98.4% (σ)	[8]
PES–NS–10%	Dense *N*-spirocyclic	2 M NaOH at 80 °C, 864 h	84.3% (σ) and 86.2% (IEC)	[9]
CP1	Dimethyl pyrrolinidium	1 M KOH at 80 °C, 720 h	60% (σ) and 55% (IEC)	[10]
PPO-7QPi-1.7	Piperidinium	1 M, NaOH at 90 C, 192 h	94% (σ)	[11]
QPEEK-*spiro*-pyr	Pyrrolinidium	1 M NaOH at 60 °C, 480 h	81.0% (σ)	[12]
QPEEK-spiro-pip	Piperidinium		74.7% (σ)	
PPO-6CH_2-3x	Poly(DAPCl)	1 M KOH at 60 °C, 336 h	92.4% (σ)	This study

*Retention in σ and/or IEC are the remaining proportions of membrane σ and/or IEC after the alkaline test at the specified conditions.

Table S2. Anion exchange membranes used in Zn-air batteries. Reproduced from ref [13].

AEM	Battery type	Electrode		Electrolyte	Peak power density (mW/cm^2)	Ref
		Zn electrode	Air electrode			
FAA-3-based AEM	Rechargeable Zn–air battery	Stainless-steel mesh coat with Zn species	Cobalt oxide based commercial	6 mol KOH PAA gel	9.8	[14]
A201-based	Solid flexible rechargeable Zn–air battery	Zn film and poly (vinylidene fluoride-cohexafluoropropene) polymer binder	Co_3O_4 nano-particles (<50 nm particle size) Gas diffusion layer: (catalyst loading of 1.0 mg/cm^2)		33	[15]
Laminated cross-linked nanocellulose/GO (QAFCGO)					44	
PPO–MPY	Primary Zn-air battery	Pure Zn plate	Ni-foam current collector and gas diffusion layer. Mixture of MnO_2 and VXC72 as catalyst.	7 M KOH	70	[16]
AEM composed of PVA/guar hydroxypropyltrimonium chloride (PGG-GP)	All-solid-state Zn–air battery	Polished Zn foil	IrO_2 and 40 wt.% Pt/C, catalyst ink, 5 wt % Nafion and ethanol	-	50	[17]
PPO-3.45 + 3501	Zn slurry-air flow battery	Zn slurry containing Zn, ZnO, Carbopol and aqueous KOH.	Catalyst ink (Pt/C catalyst with Pt loading at 1 mg/cm^2, isopropanol and deionized water)	Zn slurry	66	[18]
PPO-6CH_2-3x	Zn slurry-air flow battery	Zn slurry containing Zn, ZnO, Carbopol and aqueous KOH.	Catalyst ink (Pt/C catalyst mixed with Fumion FAA-3, deionized water and isopropanol)	Zn slurry	153	This work

References

(1) Strasser, D. J.; Graziano, B. J.; Knauss, D. M. Base Stable Poly(Diallylpiperidinium Hydroxide) Multiblock Copolymers for Anion Exchange Membranes. *J. Mater. Chem. A* **2017**, *5* (20), 9627–9640. https://doi.org/10.1039/C7TA00905D.

(2) Chen, N.; Lu, C.; Li, Y.; Long, C.; Zhu, H. Robust Poly(Aryl Piperidinium)/N-Spirocyclic Poly(2,6-Dimethyl-1,4-Phenyl) for Hydroxide-Exchange Membranes. *J. Memb. Sci.* **2019**, *572*, 246–254. https://doi.org/10.1016/j.memsci.2018.10.067.

(3) Zhang, Y.; Chen, W.; Yan, X.; Zhang, F.; Wang, X.; Wu, X.; Pang, B.; Wang, J.; He, G. Ether Spaced N-Spirocyclic Quaternary Ammonium Functionalized Crosslinked Polysulfone for High Alkaline Stable Anion Exchange Membranes. *J. Memb. Sci.* **2020**, *598*, 117650. https://doi.org/10.1016/j.memsci.2019.117650.

(4) Xue, J.; Liu, X.; Zhang, J.; Yin, Y.; Guiver, M. D. Poly(Phenylene Oxide)s Incorporating N-Spirocyclic Quaternary Ammonium Cation/Cation Strings for Anion Exchange Membranes. *J. Memb. Sci.* **2020**, *595*, 117507. https://doi.org/10.1016/j.memsci.2019.117507.

(5) Zhu, H.; Li, Y.; Chen, N.; Lu, C.; Long, C.; Li, Z.; Liu, Q. Controllable Physical-Crosslinking Poly(Arylene 6-Azaspiro[5.5] Undecanium) for Long-Lifetime Anion Exchange Membrane Applications. *J. Memb. Sci.* **2019**, *590*, 117307. https://doi.org/10.1016/j.memsci.2019.117307.

(6) Chu, X.; Liu, L.; Huang, Y.; Guiver, M. D.; Li, N. Practical Implementation of Bis-Six-Membered N-Cyclic Quaternary Ammonium Cations in Advanced Anion Exchange Membranes for Fuel Cells: Synthesis and Durability. *J. Memb. Sci.* **2019**, *578*, 239–250. https://doi.org/10.1016/j.memsci.2019.02.051.

(7) Chen, N.; Long, C.; Li, Y.; Lu, C.; Zhu, H. Ultrastable and High Ion-Conducting Polyelectrolyte Based on Six-Membered N-Spirocyclic Ammonium for Hydroxide Exchange Membrane Fuel Cell Applications. *ACS Appl. Mater. Interfaces* **2018**, *10* (18), 15720–15732. https://doi.org/10.1021/acsami.8b02884.

(8) Gu, L.; Dong, H.; Sun, Z.; Li, Y.; Yan, F. Spirocyclic Quaternary Ammonium Cations for Alkaline Anion Exchange Membrane Applications: An Experimental and Theoretical Study. *RSC Adv.* **2016**, *6* (97), 94387–94398. https://doi.org/10.1039/C6RA22313C.

(9) Liu, F. H.; Yang, Q.; Gao, X. L.; Wu, H. Y.; Zhang, Q. G.; Zhu, A. M.; Liu, Q. L. Anion Exchange Membranes with Dense N-Spirocyclic Cations as Side-Chain. *J. Memb. Sci.* **2020**, *595*, 117560. https://doi.org/10.1016/j.memsci.2019.117560.

(10) Wang, Z.; Parrondo, J.; Sankarasubramanian, S.; Bhattacharyya, K.; Ghosh, M.; Ramani, V. Alkaline Stability of Pure Aliphatic-Based Anion Exchange Membranes Containing Cycloaliphatic

Quaternary Ammonium Cations. *J. Electrochem. Soc.* **2020**, *167* (12), 124504. https://doi.org/10.1149/1945-7111/abac29.

(11) Dang, H.-S.; Jannasch, P. Alkali-Stable and Highly Anion Conducting Poly(Phenylene Oxide)s Carrying Quaternary Piperidinium Cations. *J. Mater. Chem. A* **2016**, *4* (30), 11924–11938. https://doi.org/10.1039/C6TA01905F.

(12) Shang, L.; Yao, D.; Pang, B.; Zhao, C. Anion Exchange Membranes Based on Poly (Ether Ether Ketone) Containing N-Spirocyclic Quaternary Ammonium Cations in Phenyl Side Chain. *Int. J. Hydrogen Energy* **2021**, *46* (36), 19116–19128. https://doi.org/10.1016/j.ijhydene.2021.03.059.

(13) Tsehaye, M. T.; Alloin, F.; Iojoiu, C.; Tufa, R. A.; Aili, D.; Fischer, P.; Velizarov, S. Membranes for Zinc-Air Batteries: Recent Progress, Challenges and Perspectives. *J. Power Sources* **2020**, *475*, 228689. https://doi.org/10.1016/j.jpowsour.2020.228689.

(14) Kwon, O.; Hwang, H. J.; Ji, Y.; Jeon, O. S.; Kim, J. P.; Lee, C.; Shul, Y. G. Transparent Bendable Secondary Zinc-Air Batteries by Controlled Void Ionic Separators. *Sci. Rep.* **2019**, *9* (1), 3175. https://doi.org/10.1038/s41598-019-38552-4.

(15) Zhang, J.; Fu, J.; Song, X.; Jiang, G.; Zarrin, H.; Xu, P.; Li, K.; Yu, A.; Chen, Z. Laminated Cross-Linked Nanocellulose/Graphene Oxide Electrolyte for Flexible Rechargeable Zinc-Air Batteries. *Adv. Energy Mater.* **2016**, *6* (14), 1600476. https://doi.org/10.1002/aenm.201600476.

(16) Abbasi, A.; Hosseini, S.; Somwangthanaroj, A.; Mohamad, A. A.; Kheawhom, S. Poly(2,6-Dimethyl-1,4-Phenylene Oxide)-Based Hydroxide Exchange Separator Membranes for Zinc–Air Battery. *Int. J. Mol. Sci.* **2019**, *20* (15), 3678. https://doi.org/10.3390/ijms20153678.

(17) Wang, M.; Xu, N.; Fu, J.; Liu, Y.; Qiao, J. High-Performance Binary Cross-Linked Alkaline Anion Polymer Electrolyte Membranes for All-Solid-State Supercapacitors and Flexible Rechargeable Zinc–Air Batteries. *J. Mater. Chem. A* **2019**, *7* (18), 11257–11264. https://doi.org/10.1039/C9TA02314C.

(18) Tsehaye, M. T.; Teklay Gebreslassie, G.; Heon Choi, N.; Milian, D.; Martin, V.; Fischer, P.; Tübke, J.; El Kissi, N.; Donten, M. L.; Alloin, F.; Iojoiu, C. Pristine and Modified Porous Membranes for Zinc Slurry–Air Flow Battery. *Molecules* **2021**, *26* (13), 4062. https://doi.org/10.3390/molecules26134062.